Shock Waves (2019) 29:235–261
DOI 10.1007/s00193-018-0829-x

ORIGINAL ARTICLE

Methods for compressible multiphase flows and their applications

H. Kim[1] · Y. Choe[1] · H. Kim[2] · D. Min[1] · C. Kim[1,3]

Received: 24 August 2017 / Revised: 6 April 2018 / Accepted: 26 April 2018 / Published online: 9 June 2018

Abstract This paper presents an efficient and robust numerical framework to deal with multiphase real-fluid flows and their broad spectrum of engineering applications. A homogeneous mixture model incorporated with a real-fluid equation of state and a phase change model is considered to calculate complex multiphase problems. As robust and accurate numerical methods to handle multiphase shocks and phase interfaces over a wide range of flow speeds, the AUSMPW+_N and RoeM_N schemes with a system preconditioning method are presented. These methods are assessed by extensive validation problems with various types of equation of state and phase change models. Representative realistic multiphase phenomena, including the flow inside a thermal vapor compressor, pressurization in a cryogenic tank, and unsteady cavitating flow around a wedge, are then investigated as application problems. With appropriate physical modeling followed by robust and accurate numerical treatments, compressible multiphase flow physics such as phase changes, shock discontinuities, and their interactions are well captured, confirming the suitability of the proposed numerical framework to wide engineering applications.

Communicated by D. Zeidan and H. D. Ng.

✉ C. Kim
chongam@snu.ac.kr

[1] Department of Mechanical and Aerospace Engineering, Seoul National University, 1 Gwanak-ro, Gwanak-gu, Seoul 08826, Republic of Korea

[2] Hyundai Maritime Research Institute, Hyundai Heavy Industries, 75 Yulgok-ro, Jongno-gu, Seoul 03058, Republic of Korea

[3] Institute of Advanced Aerospace Technology, Seoul National University, 1 Gwanak-ro, Gwanak-gu, Seoul 08826, Republic of Korea

Keywords Homogeneous mixture model · Low-Mach-number preconditioning · Multiphase shock capturing · Cryogenic flows · Phase change

1 Introduction

Compressible multiphase flows are found in numerous applications such as underwater explosive devices, cavitation around high-speed projectiles, phase change in desalination plants, and liquid propellant flows in rocket engines. Numerical analysis of these flows requires a suitable mathematical model representing compressible multiphase flow features. For example, the multiphase mathematical model should properly handle a phase interface and multiphase shock when dealing with the underwater explosion. For the simulation of flows with phase change, the heat exchange between phases must be accurately reflected in the multiphase model, which can be realized by fully coupling the energy equation. Also, the multiphase mathematical model should be able to readily include, if necessary, additional phase (or species) without incurring a significant increase in computational cost.

One of the well-known general multiphase models is the non-equilibrium model proposed by Baer and Nunziato [1], which solves the continuity, momentum, and energy equations for each phase, recognizing different pressures, velocities, and temperatures between phases within a computational cell. The non-equilibrium interactions at phase interfaces are taken into account by modeling the interfacial drag, heat and mass transfer, and pressure relaxation. The governing equations of this type are usually hyperbolic, but cannot be expressed in a fully conservative form, making it difficult to obtain the correct shock jump condition. Another non-equilibrium model that is hyperbolic as well as conservative has been proposed by Romenski et al. [2]. However,

solving this set of conservation laws with full interaction terms requires a significant computational cost for realistic three-dimensional applications. Depending on the nature of the problems of interest, redundant equations of the non-equilibrium model can be dropped while keeping the terms directly related to the velocity non-equilibrium process [3]. Some reduced models with the velocity and/or pressure equilibrium are widely used, and continuous efforts have been made to analyze them and to address issues associated with conservation and hyperbolicity [4–6].

On the other hand, a wide range of multiphase flows can also be described by further introducing the mechanical (velocity and pressure) and thermal (temperature) equilibrium assumptions between phases on each computational cell, which is known as the homogeneous mixture model. The homogeneous mixture approach secures the issues of conservation and hyperbolicity, ensuring the Rankine–Hugoniot shock jump condition, and thus facilitates the numerical methods developed for single-phase gas dynamics. In the homogeneous mixture model, the fluid mixture is described by one set of the continuity, momentum, and energy equations. One more continuity equation is necessary to account for the mixture composition in the metastable equilibrium induced by the different chemical potentials of the vapor and liquid phases. Turbulence effects can be incorporated by employing a turbulence model in single-phase flows, although more research on two-phase turbulence modeling is definitely necessary. Owing to relatively simple formulation, realistic three-dimensional applications can be realized when the relevant equilibrium assumptions are acceptable.

Numerous studies on multiphase problems, especially on phase change problems, have been carried out with the homogeneous mixture model [7–10]. However, applications have been mostly limited to the area of phase change flows; multiphase flows with shocks or interactions between shocks and phase interfaces have been rarely investigated with the homogeneous mixture model. The purpose of the present work is efficient and accurate computations of a broad spectrum of multiphase phenomena. Within the framework of the homogeneous mixture approach, the applicability of a numerical framework can be extended with:

- accurate numerical methods suitable to flows over a wide range of speeds,
- proper physical models for phase change,
- real-fluid properties by general equation of state (EOS).

Describing multiphase flows with the homogeneous mixture model is rather straightforward, but the numerical methods designed for single-phase flows should be substantially altered by incorporating physical and numerical issues arising from homogeneous multiphase flows. Among such issues are the lower speed of sound in a mixture, deterioration of convergence and accuracy in the low-Mach-number regions, and separate treatment for shock and phase discontinuities. Keeping these in mind, the authors have developed robust and accurate flux schemes for multiphase real-fluid flows spanning a wide range of flow speeds [11].

Since the homogeneous mixture model accompanies the relaxation of chemical potential during phase change, a proper phase change model should be implemented. In order to apply the non-equilibrium phase transition models, the EOS should cover not only the sub- and supercritical states, but also the metastable state. Furthermore, a simple mathematical formulation of EOS is not available to most real fluids such as cryogens (LH_2, LO_2, and LN_2), or liquid fuels (gasoline, kerosene, LPG, and ammonia). Therefore, it is crucial to develop a numerical framework that is fully compatible with arbitrary EOS encompassing the metastable state.

In this work, we firstly present efficient, robust, and accurate numerical methods to deal with multiphase real-fluid flows over a wide range of speeds within the framework of the homogeneous mixture model and then validate them by computing multiphase test cases extensively. Finally, we apply the validated numerical framework to practical engineering problems with their own difficulties as follows:

- nucleation in a thermal vapor compressor (TVC) which requires a non-equilibrium phase change model to simulate droplet condensation inside the TVC,
- pressurization inside a cryogenic tank, where an EOS should cover the entire regime of thermodynamic states,
- unsteady cavitating flow around a wedge which requires a well-scaled numerical flux for unsteady flows spanning from subsonic to supersonic Mach numbers.

2 Governing equations

2.1 Homogeneous mixture model

The homogeneous mixture model with mass fraction is adopted to describe multiphase flows. The compressible Reynolds-averaged Navier–Stokes equations are cast in an integral, Cartesian tensor form within an arbitrary control volume Ω with control surface $\partial\Omega$ as follows:

$$\frac{\partial}{\partial t}\int_{\Omega}\mathbf{W}\mathrm{d}\Omega+\oint_{\partial\Omega}\left[\mathbf{F}-\mathbf{F}_{\mathrm{v}}\right]\mathrm{d}S=\int_{\Omega}\mathbf{Q}_{\mathrm{pc}}\mathrm{d}\Omega. \tag{1}$$

The vector of conservative variables $\mathbf{W}$ and the convective flux vector $\mathbf{F}$ are, respectively, given by

$$\mathbf{W}=\left[\rho\quad \rho u\quad \rho v\quad \rho E\quad \rho y_{\mathrm{v}}\quad \rho y_{\mathrm{g}}\quad \rho\eta\right]^{\mathrm{T}}, \tag{2}$$

$$\mathbf{F} = [\rho U \quad \rho u U + n_x p \quad \rho v U + n_y p \quad \rho H U \quad \rho y_\mathrm{v} U \quad \rho y_\mathrm{g} U \quad \rho \eta U]^\mathrm{T}. \tag{3}$$

$\mathbf{F}_\mathrm{v}$ indicates the viscous flux vector, and $\mathbf{Q}_\mathrm{pc}$ is the vector of the phase change source term. Note that the equation of $\rho\eta$ is included only if the nucleation-theory-based model is employed as a phase change model, which will be handled in Sect. 2.3. In (3), $U(\equiv n_x u + n_y v)$ is the contravariant velocity component normal to the surface element $\mathrm{d}S$. The mass fractions satisfy the following constitutive relation:

$$y_\mathrm{l} + y_\mathrm{v} + y_\mathrm{g} = 1, \tag{4}$$

where the subscripts (l, v, g) signify the liquid, vapor, and non-condensable gas phases, respectively.

The speed of sound of a mixture is evaluated from the following definition:

$$c^2 \equiv \left.\frac{\partial p}{\partial \rho}\right|_s = \frac{\rho \frac{\partial h}{\partial T}}{\rho \frac{\partial \rho}{\partial p}\frac{\partial h}{\partial T} + \frac{\partial \rho}{\partial T}\left(1 - \rho \frac{\partial h}{\partial p}\right)}. \tag{5}$$

The density and derivative values of the mixture are determined from the definitions of mixture density and enthalpy (7, 8). For example,

$$\frac{\partial \rho}{\partial p} = \rho^2 \left(\frac{1 - y_\mathrm{v} - y_\mathrm{g}}{\breve{\rho}_\mathrm{l}^2} \left.\frac{\partial \breve{\rho}_\mathrm{l}}{\partial p}\right|_T + \frac{y_\mathrm{v}}{\breve{\rho}_\mathrm{v}^2} \left.\frac{\partial \breve{\rho}_\mathrm{v}}{\partial p}\right|_T + \frac{y_\mathrm{g}}{\breve{\rho}_\mathrm{g}^2} \left.\frac{\partial \breve{\rho}_\mathrm{g}}{\partial p}\right|_T \right), \tag{6}$$

where the derivatives of each phase are obtained from the respective EOS of each phase. The left-hand side of (6) is evaluated under constant T, y_v, y_g conditions. Figure 1 shows that the mixture speed of sound obtained by (5) is lower than Wood's speed of sound (speed of sound from the mechanical equilibrium mixture), indicating that the homogeneous mixture model satisfies the subcharacteristic condition with respect to the mechanical equilibrium model [12].

2.2 Equation of state (EOS)

The mixture density is defined as follows:

$$\frac{1}{\rho} = \frac{(1 - y_\mathrm{v} - y_\mathrm{g})}{\breve{\rho}_\mathrm{l}} + \frac{y_\mathrm{v}}{\breve{\rho}_\mathrm{v}} + \frac{y_\mathrm{g}}{\breve{\rho}_\mathrm{g}}. \tag{7}$$

Here, $\breve{q}$ indicates the quantity q defined by Amagat's law. The mixture enthalpy h is calculated as

$$h = h_\mathrm{l}(1 - y_\mathrm{v} - y_\mathrm{g}) + h_\mathrm{v} y_\mathrm{v} + h_\mathrm{g} y_\mathrm{g}. \tag{8}$$

The system is then closed by including an EOS for the constituent phases. All thermodynamic properties of each phase

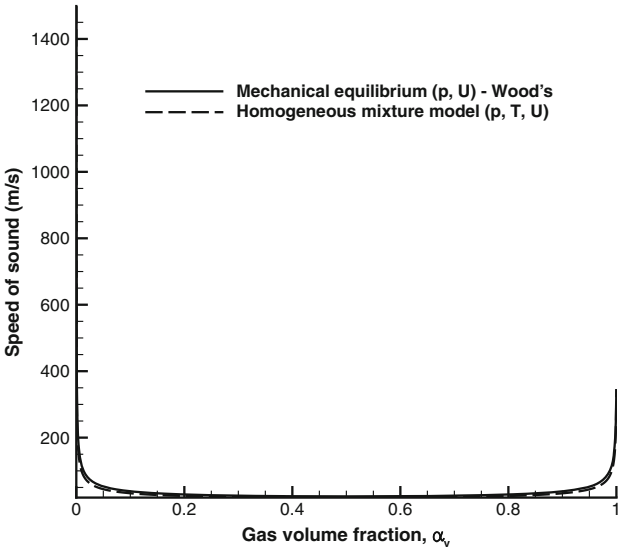

Fig. 1 Comparison of speed of sound

are generated as functions of the local pressure p and temperature T as follows:

$$\breve{\rho}_i = \breve{\rho}_i(p, T), \quad h_i = h_i(p, T), \quad (i = \mathrm{l},\ \mathrm{v},\ \mathrm{g}). \tag{9}$$

We use various relations between the thermodynamic properties (ρ, h) and the independent variables (p, T).

In order to adopt the same EOS used in the reference paper of each validation case, the non-condensable gas phase is described by an ideal gas EOS and the liquid phase of water is approximated by the stiffened gas model [13] for air–water flows without phase change. An EOS for phase change flows is chosen to reflect real-fluid properties and to cover metastable states as well. In the phase change problems of water, the liquid and vapor phases are described by the IAPWS97 formulation [14].

For real fluids, all thermodynamic properties of both liquid and vapor phases are generated from the Standard Reference Database 23, available from the National Institute of Standards and Technology (NIST) [15]. To access these thermodynamic properties efficiently, we express the density and enthalpy as functions of the local pressure and temperature by the spline-based table look-up method (SBTL) [16]. This method creates biquadratic spline functions for describing the intermediate regions between the data points that are generated from the NIST database. All coefficients of each spline function are C^1 continuous across every data point.

2.3 Phase change models

The present work describes the non-equilibrium phase change process by adding source terms as follows:

$$\mathbf{Q}_\mathrm{pc} = \begin{bmatrix} 0 & 0 & 0 & 0 & \dot{m}_\mathrm{vp} - \dot{m}_\mathrm{cd} & 0 \end{bmatrix}^\mathrm{T}. \tag{10}$$

The vaporization and condensation rates, $\dot{m}_{\mathrm{vp}}$ and $\dot{m}_{\mathrm{cd}}$, are expressed in various forms in the literature. For example, Merkle [17] defines the rates as:

$$\dot{m}_{\mathrm{vp}} = C_{\mathrm{vp}} \frac{\max(p_{\mathrm{sat}} - p, 0)}{0.5\rho_\infty V_\infty^2 t_\infty} \check{\rho}_{\mathrm{l}} \alpha_{\mathrm{l}}, \tag{11}$$

$$\dot{m}_{\mathrm{cd}} = C_{\mathrm{cd}} \frac{\max(p - p_{\mathrm{sat}}, 0)}{0.5\rho_\infty V_\infty^2 t_\infty} \check{\rho}_{\mathrm{v}} \alpha_{\mathrm{v}}, \tag{12}$$

where ρ_∞ and V_∞ are the free stream mixture density and mixture velocity, respectively. Here, t_∞ denotes the reference time scale, usually defined by the characteristic length divided by V_∞. The Schnerr–Sauer model [18] is given by:

$$\dot{m}_{\mathrm{vp}} = \frac{3\alpha_{\mathrm{v}}(1-\alpha_{\mathrm{v}})}{\mathscr{R}_{\mathrm{B}}} \frac{\check{\rho}_{\mathrm{v}}\check{\rho}_{\mathrm{l}}}{\rho} \sqrt{\frac{2}{3}\frac{(p_{\mathrm{sat}} - p)}{\check{\rho}_{\mathrm{l}}}} \quad \text{if } p < p_{\mathrm{sat}}, \tag{13}$$

$$\dot{m}_{\mathrm{cd}} = \frac{3\alpha_{\mathrm{v}}(1-\alpha_{\mathrm{v}})}{\mathscr{R}_{\mathrm{B}}} \frac{\check{\rho}_{\mathrm{v}}\check{\rho}_{\mathrm{l}}}{\rho} \sqrt{\frac{2}{3}\frac{(p - p_{\mathrm{sat}})}{\check{\rho}_{\mathrm{l}}}} \quad \text{if } p \geq p_{\mathrm{sat}}. \tag{14}$$

The bubble radius is given by $\mathscr{R}_{\mathrm{B}} = \left(\frac{\alpha_{\mathrm{v}}}{1-\alpha_{\mathrm{v}}}\frac{3}{4\pi n}\right)^{1/3}$, and the bubble number density (n) is set to 10^9 for all computations. When the Hertz–Knudsen-equation-based model [19] is used, phase change rates are expressed as

$$\dot{m}_{\mathrm{vp}} = C_{\mathrm{vp}} \frac{\max(p_{\mathrm{sat}} - p, 0)}{\sqrt{2\pi R_{\mathrm{u}} T}} \check{\rho}_{\mathrm{l}} \alpha_{\mathrm{l}}, \tag{15}$$

$$\dot{m}_{\mathrm{cd}} = C_{\mathrm{cd}} \frac{\max(p - p_{\mathrm{sat}}, 0)}{\sqrt{2\pi R_{\mathrm{u}} T}} \check{\rho}_{\mathrm{v}} \alpha_{\mathrm{v}}. \tag{16}$$

Here, R_{u} is the universal gas constant. In the above phase change rates, C_{cd} and C_{vp} indicate the accommodation coefficients for condensation and vaporization, respectively. Depending on whether the local pressure is lower/higher than the saturation pressure, the conversion from liquid/vapor to vapor/liquid appears at the vaporization/condensation rate of $\dot{m}_{\mathrm{vp}}, \dot{m}_{\mathrm{cd}}$, respectively. In order to capture the effect of nucleation and droplet distribution accurately, we also employ a phase change model based on the classical nucleation theory. The nucleation-theory-based model considers the pressure deviation from the saturation point and the droplet distribution [20], and hence, it solves an additional transport equation for the droplet number density (η) in the governing equations. The phase change source term is then expressed as

$$\mathbf{Q}_{\mathrm{pc}} = \left[0 \quad 0 \quad 0 \quad 0 \quad -\left(\dot{m}_{\mathrm{gen}} + \dot{m}_{\mathrm{growth}}\right) \quad 0 \quad \rho I\right]^{\mathrm{T}}, \tag{17}$$

where $\dot{m}_{\mathrm{gen}}$ and $\dot{m}_{\mathrm{growth}}$ stand for phase change rates due to the generation and the growth/demise of droplets, respectively. They are defined as follows:

$$\dot{m}_{\mathrm{gen}} = \frac{4}{3}\pi\check{\rho}_{\mathrm{l}} I r^{*3}, \quad \dot{m}_{\mathrm{growth}} = 4\pi\check{\rho}_{\mathrm{l}} r^2 \eta \frac{\partial r}{\partial t}, \tag{18}$$

where I and $\partial r/\partial t$ denote the nucleation rate and droplet growth rate, respectively. Detailed formulations can be found in Ref. [20].

2.4 Turbulence model

A turbulence model based on the Boussinesq hypothesis relates the Reynolds stress with the eddy viscosity μ_{T}. The role of such first-order turbulence closures is to compute the eddy viscosity μ_{T} properly. Among a large variety of first-order closure models, we choose the $k-\omega$ SST (shear stress transport) two-equation model [21]. When the problems of interest need to take turbulence effects into account, the following turbulence transport equations are added to the governing equations (1). In the present work, the turbulence equations are decoupled from the mean-flow equations to realize the numerical treatment of the turbulence transport and mean-flow equations flexibly.

– Turbulent kinetic energy (k) equation

$$\frac{\partial}{\partial t}(\rho k) + \frac{\partial}{\partial x_j}\left(\rho u_j k\right) - \frac{\partial}{\partial x_j}\left[(\mu + \sigma_k \mu_{\mathrm{T}})\frac{\partial k}{\partial x_j}\right] = Q_{\mathrm{T},k}. \tag{19}$$

– Turbulent dissipation rate (ω) equation

$$\frac{\partial}{\partial t}(\rho \omega) + \frac{\partial}{\partial x_j}\left(\rho u_j \omega\right) - \frac{\partial}{\partial x_j}\left[(\mu + \sigma_\omega \mu_{\mathrm{T}})\frac{\partial \omega}{\partial x_j}\right] = Q_{\mathrm{T},\omega}. \tag{20}$$

The vector of conservative variables (2) and convective flux vector (3) are then given by

$$\mathbf{W} = \left[\rho \quad \rho u \quad \rho v \quad \rho E \quad \rho y_{\mathrm{v}} \quad \rho y_{\mathrm{g}} \quad \rho k \quad \rho\omega\right]^{\mathrm{T}}, \tag{21}$$

$$\mathbf{F} = [\ \rho U \quad \rho u U + n_x p \quad \rho v U + n_y p \quad \rho H U \quad \rho y_{\mathrm{v}} U \quad \rho y_{\mathrm{g}} U \quad \rho k U \quad \rho\omega U\ ]^{\mathrm{T}}. \tag{22}$$

In (19) and (20), the source terms $Q_{\mathrm{T},k}$ and $Q_{\mathrm{T},\omega}$ are given as follows:

$$Q_{\mathrm{T},k} = \tilde{P} - \beta_{\mathrm{T}}^* \rho\omega k, \tag{23}$$

$$Q_{\mathrm{T},\omega} = \frac{C_\omega \rho}{\mu_{\mathrm{T}}}\tilde{P} - \beta_{\mathrm{T}}\rho\omega^2 + 2\rho(1-F_1)\frac{\sigma_{\omega 2}}{\omega}\frac{\partial k}{\partial x_j}\frac{\partial \omega}{\partial x_j}. \tag{24}$$

Here, $\tilde{P}$ represents the production term for k, F_1 is the blending function, and μ_T is given by

$$\mu_T = \frac{a_1 \rho k}{\max(a_1 \omega, f_2 \sqrt{2 S_{ij} S_{ij}})}. \tag{25}$$

More details and the values of each coefficient in the $k-\omega$ SST model can be found in Ref. [21].

2.5 System preconditioning

In general, numerical methods for compressible flows possess good stability and convergence characteristics in high-speed compressible flow regimes. At low speeds, however, the convergence rates are known to be significantly deteriorated by system stiffness resulting from the disparate convective and acoustic velocities. The convergence rates can be made independent of the Mach number by altering the acoustic speed of the system such that all eigenvalues are of the same order and thus the condition number approaches unity. In order to precondition the governing equations (1), we pre-multiply the time derivative term by the preconditioning matrix of Weiss and Smith [22] as follows:

$$\boldsymbol{\Gamma} \frac{\partial}{\partial \tau} \int_\Omega \mathbf{Q} \mathrm{d}\Omega + \oint_{\partial\Omega} [\mathbf{F} - \mathbf{F}_\mathrm{v}] \, \mathrm{d}S = \int_\Omega \mathbf{Q}_\mathrm{pc} \mathrm{d}\Omega. \tag{26}$$

Here, $\mathbf{Q}$ indicates the primitive variable vector given by

$$\mathbf{Q} = \begin{bmatrix} p & u & v & T & y_\mathrm{v} & y_\mathrm{g} & k & \omega \end{bmatrix}^\mathrm{T}, \tag{27}$$

and the preconditioning matrix $\boldsymbol{\Gamma}$ is

$$\boldsymbol{\Gamma} = \begin{bmatrix} \frac{1}{\beta} & 0 & 0 & \frac{\partial \rho}{\partial T} & \frac{\partial \rho}{\partial y_\mathrm{v}} & \frac{\partial \rho}{\partial y_\mathrm{g}} & 0 & 0 \\ \frac{u}{\beta} & \rho & 0 & \frac{\partial \rho}{\partial T} u & \frac{\partial \rho}{\partial y_\mathrm{v}} u & \frac{\partial \rho}{\partial y_\mathrm{g}} u & 0 & 0 \\ \frac{v}{\beta} & 0 & \rho & \frac{\partial \rho}{\partial T} v & \frac{\partial \rho}{\partial y_\mathrm{v}} v & \frac{\partial \rho}{\partial y_\mathrm{g}} v & 0 & 0 \\ H^* & \rho u & \rho v & \frac{\partial \rho}{\partial T} H + \rho \frac{\partial h}{\partial T} & \frac{\partial \rho}{\partial y_\mathrm{v}} H + \rho \frac{\partial h}{\partial y_\mathrm{v}} & \frac{\partial \rho}{\partial y_\mathrm{g}} H + \rho \frac{\partial h}{\partial y_\mathrm{g}} & 0 & 0 \\ \frac{y_\mathrm{v}}{\beta} & 0 & 0 & \frac{\partial \rho}{\partial T} y_\mathrm{v} & \frac{\partial \rho}{\partial y_\mathrm{v}} y_\mathrm{v} + \rho & \frac{\partial \rho}{\partial y_\mathrm{g}} y_\mathrm{v} & 0 & 0 \\ \frac{y_\mathrm{g}}{\beta} & 0 & 0 & \frac{\partial \rho}{\partial T} y_\mathrm{g} & \frac{\partial \rho}{\partial y_\mathrm{v}} y_\mathrm{g} & \frac{\partial \rho}{\partial y_\mathrm{g}} y_\mathrm{g} + \rho & 0 & 0 \\ \frac{k}{\beta} & 0 & 0 & \frac{\partial \rho}{\partial T} k & \frac{\partial \rho}{\partial y_\mathrm{v}} k & \frac{\partial \rho}{\partial y_\mathrm{g}} k & \rho & 0 \\ \frac{\omega}{\beta} & 0 & 0 & \frac{\partial \rho}{\partial T} \omega & \frac{\partial \rho}{\partial y_\mathrm{v}} \omega & \frac{\partial \rho}{\partial y_\mathrm{g}} \omega & 0 & \rho \end{bmatrix} \tag{28}$$

with

$$H^* = \frac{H}{\beta} + \rho \frac{\partial h}{\partial p} - 1. \tag{29}$$

If $1/\beta$ becomes $\frac{\partial \rho}{\partial p}$, then $\boldsymbol{\Gamma}$ reverts to the Jacobian matrix $\frac{\partial \mathbf{W}}{\partial \mathbf{Q}}$, resulting in the non-preconditioned system in the primitive form. The eigenvalues of the preconditioned system in (26) are given by

$$\lambda \left(\boldsymbol{\Gamma}^{-1} \frac{\partial \mathbf{F}}{\partial \mathbf{Q}} \right) = U' - D, U' + D, U, U, U, U, U, U. \tag{30}$$

Here,

$$U' = \frac{1}{2} \left(1 + \frac{c'^2}{c^2} \right) U, \tag{31}$$

$$D = \frac{1}{2} \sqrt{\left(1 - \frac{c'^2}{c^2} \right)^2 U^2 + 4 c'^2}. \tag{32}$$

The terms $1/\beta$ and c' are related by

$$\frac{1}{\beta} = \frac{1}{c'^2} - \frac{\frac{\partial \rho}{\partial T} \left(1 - \rho \frac{\partial h}{\partial p} \right)}{\rho \frac{\partial h}{\partial T}}. \tag{33}$$

The preconditioned speed of sound c' is then given by

$$c' = \min \left(c, \max \left(\sqrt{u^2 + v^2}, V_\mathrm{co} \right) \right). \tag{34}$$

In (34), V_co is a cutoff value that prevents the local velocity from zero in the vicinity of the stagnation region. The cutoff parameter V_co is generally specified as $V_\mathrm{co} = k V_\infty$. We set $k = 1$ in every computation of low-speed flow or flow where incompressible and compressible regions coexist. In supersonic flows, the preconditioned speed of sound becomes the local speed of sound, meaning that the preconditioning is turned off.

In low-Mach-number unsteady flows, the unsteady preconditioned speed of sound is given by

$$c'_\mathrm{un} = \min \left(c, \max \left(\sqrt{u^2 + v^2}, V_\mathrm{co}, V_\mathrm{un} \right) \right). \tag{35}$$

Here, the unsteady preconditioning parameter V_un accounts for the effect of the Strouhal number [23] as follows:

$$V_\mathrm{un} = \frac{L}{\pi \Delta t} = \frac{L}{\pi \Delta t V} \times V = \mathrm{St} \times V, \tag{36}$$

where L is a characteristic length scale and Δt is the physical time step. The characteristic length scale is typically taken as the problem domain size, a representative length scale of the lowest wave number. Equation 36 is derived for single-phase gas flows, but it is applicable to multiphase flows because the multiphase effects described by the homogeneous mixture equations simply change the magnitude of the speed of sound.

3 Numerical methods

We introduce the flux schemes for homogeneous multiphase real-fluid flows over a wide range of speeds. Robust and accurate shock-capturing schemes originally developed for single-phase gas dynamics, AUSMPW+ [24] and RoeM [25],

have been extended to AUSMPW+_N and RoeM_N, respectively, for multiphase real-fluid flows with general EOSs. The extended schemes have proven to be robust and accurate without compromising the accuracy of the original schemes. Detailed derivation and discussion on the features of both schemes can be found in Ref. [11].

3.1 AUSMPW+_N

Within the framework of standard finite volume discretization, the numerical flux of AUSMPW+_N at a cell-interface is given by:

$$\mathbf{F}_{1/2} = \bar{\mathscr{M}}_{\mathrm{L}}^{+} c_{1/2} \boldsymbol{\psi}_{\mathrm{L}} + \bar{\mathscr{M}}_{\mathrm{R}}^{-} c_{1/2} \boldsymbol{\psi}_{\mathrm{R}} + \mathbf{p}_{1/2}. \tag{37}$$

Here, $\boldsymbol{\psi}$ and $\mathbf{p}_{1/2}$ are given by

$$\boldsymbol{\psi} = [\rho \quad \rho u \quad \rho v \quad \rho H \quad \rho y_{\mathrm{v}} \quad \rho y_{\mathrm{g}} \quad \rho k \quad \rho\omega]^{\mathrm{T}}, \tag{38}$$

$$\mathbf{p}_{1/2} = [0 \quad n_x p_{1/2} \quad n_y p_{1/2} \quad 0 \quad 0 \quad 0 \quad 0 \quad 0]^{\mathrm{T}}. \tag{39}$$

The pressure flux is

$$p_{1/2} = \mathscr{P}_{\mathrm{L}}^{+} p_{\mathrm{L}} + \mathscr{P}_{\mathrm{R}}^{-} p_{\mathrm{R}} + p_u. \tag{40}$$

From the AUSM^{+}-up scheme [26], the velocity-difference flux term is given by

$$p_u = -2K_u \mathscr{P}_{\mathrm{L}}^{+} \mathscr{P}_{\mathrm{R}}^{-} \rho_{1/2} c_{1/2} \left(U_{\mathrm{R}} - U_{\mathrm{L}}\right). \tag{41}$$

Here, $0 \le K_u \le 1$, and we set $K_u = 0.5$ in all calculations. In (37), $\bar{\mathscr{M}}_{\mathrm{L,R}}^{\pm}$ are defined as follows:
if $M_{1/2} \ge 0$,

$$\bar{\mathscr{M}}_{\mathrm{L}}^{+} = \mathscr{M}_{\mathrm{L}}^{+} + \mathscr{M}_{\mathrm{R}}^{-}[(1-w)(1+f_{\mathrm{R}}) - f_{\mathrm{L}}], \tag{42}$$

$$\bar{\mathscr{M}}_{\mathrm{R}}^{-} = \mathscr{M}_{\mathrm{R}}^{-} w(1+f_{\mathrm{R}}). \tag{43}$$

If $M_{1/2} < 0$,

$$\bar{\mathscr{M}}_{\mathrm{L}}^{+} = \mathscr{M}_{\mathrm{L}}^{+} w(1+f_{\mathrm{L}}), \tag{44}$$

$$\bar{\mathscr{M}}_{\mathrm{R}}^{-} = \mathscr{M}_{\mathrm{R}}^{-} + \mathscr{M}_{\mathrm{L}}^{+}[(1-w)(1+f_{\mathrm{L}}) - f_{\mathrm{R}}], \tag{45}$$

where $M_{1/2} = \mathscr{M}_{\mathrm{L}}^{+} + \mathscr{M}_{\mathrm{R}}^{-}$. The Mach number and pressure splitting functions at a cell-interface, $\mathscr{M}_{\mathrm{L,R}}^{\pm}$ and $\mathscr{P}_{\mathrm{L,R}}^{\pm}$, are obtained using the Mach number of each side $M_{\mathrm{L,R}} = U_{\mathrm{L,R}}/c_{1/2}$ as follows:

$$\mathscr{M}^{\pm} = \begin{cases} \pm\frac{1}{4}(M \pm 1)^2 & |M| \le 1 \\ \frac{1}{2}(M \pm |M|) & |M| > 1, \end{cases} \tag{46}$$

$$\mathscr{P}^{\pm} = \begin{cases} \pm\frac{1}{4}(M \pm 1)^2 (2 \mp M) \pm \alpha M \left(M^2 - 1\right)^2 & |M| \le 1 \\ \frac{1}{2}(1 \pm \mathrm{sign}\,(M)) & |M| > 1. \end{cases} \tag{47}$$

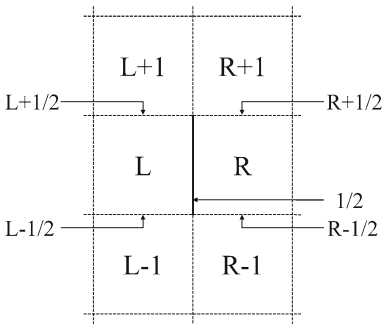

Fig. 2 Interface of a two-dimensional cell

In order to prevent unwanted near-wall oscillations and overshoots behind a strong shock, AUSMPW+_N invokes pressure-based weighting functions that provide a numerical dissipation proportional to the local pressure difference. The pressure-based weighting functions f and w (originally, symbolized as ω, but here w is used not to be confused with the turbulent dissipation rate) in (42)–(45) are defined as

$$f_{\mathrm{L,R}} = \left(\frac{p_{\mathrm{L,R}} + \rho_{1/2} c_{1/2}^2}{\rho_{1/2} c_{1/2}^2} - 1\right)(1-w)\frac{\rho_{1/2}}{\rho_{\mathrm{L/R}}}, \tag{48}$$

$$w = \max(w_1, w_2), \tag{49}$$

where

$$(\,)_{\mathrm{L/R}} = \begin{cases} (\,)_{\mathrm{L}} & M_{1/2} \ge 0 \\ (\,)_{\mathrm{R}} & M_{1/2} < 0. \end{cases} \tag{50}$$

Here, $w_1 = 1 - \Pi_{1/2}^3$, and w_2 is given by

$$w_2 = 1 - \left(\frac{\min\left(\bar{p}_{\mathrm{L}+1}, \bar{p}_{\mathrm{R}+1}, \bar{p}_{\mathrm{L}-1}, \bar{p}_{\mathrm{R}-1}\right)}{\max\left(\bar{p}_{\mathrm{L}+1}, \bar{p}_{\mathrm{R}+1}, \bar{p}_{\mathrm{L}-1}, \bar{p}_{\mathrm{R}-1}\right)}\right)^2. \tag{51}$$

Figure 2 shows the computational stencil of w_2. The weighting functions include a shock-discontinuity-sensing term $\Pi_{1/2}$ which plays a crucial role in capturing the multiphase shock discontinuity. The shock-discontinuity-sensing term Π and modified pressure $\bar{p}$ in the above equations are formulated as follows:

$$\Pi_{1/2} = \min\left(\frac{\bar{p}_{\mathrm{L}}}{\bar{p}_{\mathrm{R}}}, \frac{\bar{p}_{\mathrm{R}}}{\bar{p}_{\mathrm{L}}}\right) \tag{52}$$

with

$$\bar{p}_{\mathrm{L,R}} = p_{\mathrm{L,R}} + 0.1 \times \min\left(\rho_{\mathrm{L}} c_{\mathrm{L}}^2, \rho_{\mathrm{R}} c_{\mathrm{R}}^2\right). \tag{53}$$

To accurately capture the shock discontinuity, an AUSM-type scheme requires prudent choice of the numerical speed of sound at a cell-interface $c_{1/2}$. The Prandtl relation in gas dynamics does not hold in general two-phase flows, so the

speed of sound in the original AUSMPW+ scheme is not applicable. In AUSMPW+_N, the interfacial speed of sound is evaluated from (5) using the Roe-averaged pressure, temperature, and mass fractions. The resultant $c_{1/2}$ is consistent with the physical speed of sound in mixture flows [27].

For unsteady low-Mach-number flow calculations, the velocity- and pressure-difference dissipation fluxes should be independently scaled. The velocity-difference pressure flux (41) is scaled by the velocity scaling function (ϕ_u) as follows:

$$p^*_{1/2} = \mathscr{P}^+_{\mathrm{L}} p_{\mathrm{L}} + \mathscr{P}^-_{\mathrm{R}} p_{\mathrm{R}} + p^*_u, \quad p^*_u = \phi_u p_u \tag{54}$$

with α required in (47) given by

$$\alpha = \frac{3}{16}\left(-4 + 5\phi_u^2\right) \in \left[-\frac{3}{4}, \frac{3}{16}\right]. \tag{55}$$

Here,

$$\phi_u = \theta_u \left(2 - \theta_u\right), \tag{56}$$

and θ_u is defined by

$$\theta_u = \min\left(1, \max\left(\frac{\sqrt{u^2_{1/2} + v^2_{1/2}}}{c_{1/2}}, \frac{V_{\mathrm{co}}}{c_{1/2}}\right)\right). \tag{57}$$

Next, the pressure-difference term (48) is scaled by the pressure scaling function (ϕ_p) as follows:

$$f^*_{\mathrm{L,R}} = \frac{1}{\phi_p} f_{\mathrm{L,R}}, \tag{58}$$

with

$$\phi_p = \theta_p \left(2 - \theta_p\right). \tag{59}$$

Here, θ_p is given by

$$\theta_p = \min\left(1, \max\left(\frac{\sqrt{u^2_{1/2} + v^2_{1/2}}}{c_{1/2}}, \frac{V_{\mathrm{co}}}{c_{1/2}}, \frac{V_{\mathrm{un}}}{c_{1/2}}\right)\right). \tag{60}$$

The numerical flux (37) scaled with (54) and (58) yields the correct asymptotic behavior in the sense that the AUSMPW+_N scheme stably approaches the incompressible limit, as $M_{\mathrm{L,R}}$ (or equivalently, the free stream Mach number) $\to 0$.

3.2 RoeM_N

The RoeM_N scheme for multiphase real-fluid flows at a cell-interface is expressed as follows:

$$\mathbf{F}_{1/2} = \frac{b_1\mathbf{F}_{\mathrm{L}} - b_2\mathbf{F}_{\mathrm{R}}}{b_1 - b_2} + \frac{b_1 b_2}{b_1 - b_2} \times \left(\Delta\mathbf{W}' - \frac{g}{1 + \left|\tilde{M}\right|}\mathbf{B}\Delta\mathbf{W}'\right). \tag{61}$$

Here, $\Delta\mathbf{W}'$ and $\mathbf{B}\Delta\mathbf{W}'$ are, respectively, given by

$$\Delta\mathbf{W}' = [\Delta(\rho) \quad \Delta(\rho u) \quad \Delta(\rho v) \quad \Delta(\rho H) \quad \Delta(\rho y_{\mathrm{v}}) \quad \Delta\left(\rho y_{\mathrm{g}}\right) \quad \Delta(\rho k) \quad \Delta(\rho\omega)]^{\mathrm{T}}, \tag{62}$$

$$\mathbf{B}\Delta\mathbf{W}' = \Delta\rho \begin{pmatrix} 1 \\ \hat{u} \\ \hat{v} \\ \hat{H} \\ \hat{y}_{\mathrm{v}} \\ \hat{y}_{\mathrm{g}} \\ \hat{k} \\ \hat{\omega} \end{pmatrix} - \frac{f\Delta p}{\hat{c}^2} \begin{pmatrix} 1 \\ \hat{u} \\ \hat{v} \\ \hat{H} \\ \hat{y}_{\mathrm{v}} \\ \hat{y}_{\mathrm{g}} \\ \hat{k} \\ \hat{\omega} \end{pmatrix} + \hat{\rho} \begin{pmatrix} 0 \\ \Delta u \\ \Delta v \\ \Delta H \\ \Delta y_{\mathrm{v}} \\ \Delta y_{\mathrm{g}} \\ \Delta k \\ \Delta\omega \end{pmatrix} + \hat{\rho}\Delta U \begin{pmatrix} 0 \\ -n_x \\ -n_y \\ 0 \\ 0 \\ 0 \\ 0 \\ 0 \end{pmatrix}. \tag{63}$$

In (61), $\tilde{M}$ is given by

$$\tilde{M} = \mathrm{sign}\left(\frac{\hat{U}}{\hat{c}}\right) \times \min\left(1, \left|\frac{\hat{U}}{\hat{c}}\right|\right), \tag{64}$$

where the caret ($\hat{}$) denotes the Roe-averaged value.

To prevent an expansion shock without diffusing contact discontinuity, the following signal velocities are introduced:

$$b_1 = \max\left(0, \hat{U} + \hat{c}, U_{\mathrm{R}} + \hat{c}\right), \tag{65}$$

$$b_2 = \min\left(0, \hat{U} - \hat{c}, U_{\mathrm{L}} - \hat{c}\right). \tag{66}$$

The Mach-number-based control functions f and g to cure the shock instability are then introduced as follows:

$$f = \begin{cases} 1 & \hat{u}^2 + \hat{v}^2 = 0 \\ |\hat{M}|^h & \text{elsewhere,} \end{cases} \tag{67}$$

$$g = \begin{cases} 1 & \hat{M} = 0 \\ |\hat{M}|^{1-\Pi_{1/2}} & \hat{M} \neq 0. \end{cases} \tag{68}$$

Here, $\hat{M} = \hat{U}/\hat{c}$, and h is given by

$$h = 1 - \min\left(\Pi_{1/2}, \Pi_{\mathrm{L}+1/2}, \Pi_{\mathrm{R}+1/2}, \Pi_{\mathrm{L}-1/2}, \Pi_{\mathrm{R}-1/2}\right). \tag{69}$$

The computational stencil for h is the same as in Fig. 2, and the same shock-discontinuity-sensing term ($\Pi_{1/2}$, 52) is used for the RoeM_N scheme. Based on the linear perturbation analysis [25], f is designed to damp out the feeding rate of the pressure perturbation into the density field, and g is designed to control the damping rate of the density and the pressure perturbation. The multidimensional dissipation provided by f and g prevents the shock instability triggered by the pressure-difference term in the mass flux of the original Roe scheme.

Similar to the AUSMPW+_N scheme, the velocity- and pressure-difference dissipation fluxes are independently scaled for unsteady low-Mach-number flow calculations. The pressure-difference dissipation term (the second term on the right-hand side in (63)) is scaled by the pressure scaling function (59) as follows:

$$\frac{f\Delta p}{\hat{c}^2} \rightarrow \frac{1}{\phi_p}\frac{f\Delta p}{\hat{c}^2}. \tag{70}$$

Next, the speed of sound associated with the velocity-difference dissipation term (the last term on the right-hand side in (63)) is scaled by the velocity scaling function (56) as follows:

$$b_{1_u} = \max\left(0, \hat{U} + \phi_u\hat{c}, U_{\mathrm{R}} + \phi_u\hat{c}\right), \tag{71}$$

$$b_{2_u} = \min\left(0, \hat{U} - \phi_u\hat{c}, U_{\mathrm{L}} - \phi_u\hat{c}\right), \tag{72}$$

$$\tilde{M}_u = \mathrm{sign}\left(\frac{\hat{U}}{\phi_u\hat{c}}\right) \times \min\left(1, \left|\frac{\hat{U}}{\phi_u\hat{c}}\right|\right). \tag{73}$$

The resulting RoeM_N is then given by

$$\mathbf{F}_{1/2} = \frac{b_1\mathbf{F}_{\mathrm{L}} - b_2\mathbf{F}_{\mathrm{R}}}{b_1 - b_2} + \frac{b_1 b_2}{b_1 - b_2}\left(\Delta\mathbf{W}' - \frac{g}{1+\left|\tilde{M}\right|}\mathbf{B}\Delta\mathbf{W}'_{\mathbf{1}}\right) - \frac{b_{1_u}b_{2_u}}{b_{1_u} - b_{2_u}}\frac{g}{1+\left|\tilde{M}_u\right|}\mathbf{B}\Delta\mathbf{W}'_{\mathbf{2}}. \tag{74}$$

In (74), $\mathbf{B}\Delta\mathbf{W}'$ (61) has been split into two parts to highlight the velocity-difference term ($\mathbf{B}\Delta\mathbf{W}'_{\mathbf{2}}$) and the other part containing the pressure-difference term ($\mathbf{B}\Delta\mathbf{W}'_{\mathbf{1}}$) as follows:

$$\mathbf{B}\Delta\mathbf{W}'_{\mathbf{1}} = \Delta\rho\begin{pmatrix}1\\ \hat{u}\\ \hat{v}\\ \hat{H}\\ \hat{y}_{\mathrm{v}}\\ \hat{y}_{\mathrm{g}}\\ \hat{k}\\ \hat{\omega}\end{pmatrix} - \frac{1}{\phi_p}\frac{f\Delta p}{\hat{c}^2}\begin{pmatrix}1\\ \hat{u}\\ \hat{v}\\ \hat{H}\\ \hat{y}_{\mathrm{v}}\\ \hat{y}_{\mathrm{g}}\\ \hat{k}\\ \hat{\omega}\end{pmatrix} + \hat{\rho}\begin{pmatrix}0\\ \Delta u\\ \Delta v\\ \Delta H\\ \Delta y_{\mathrm{v}}\\ \Delta y_{\mathrm{g}}\\ \Delta k\\ \Delta\omega\end{pmatrix}, \tag{75}$$

$$\mathbf{B}\Delta\mathbf{W}'_{\mathbf{2}} = \hat{\rho}\Delta U\begin{pmatrix}0\\ -n_x\\ -n_y\\ 0\\ 0\\ 0\\ 0\\ 0\end{pmatrix}. \tag{76}$$

Like the AUSMPW+_N scheme, the RoeM_N scheme (74) scaled with (70)–(73) stably approaches the incompressible limit, as $\hat{M}$ (or equivalently, the free stream Mach number) $\rightarrow 0$.

4 Validation

The accuracy and robustness of the AUSMPW+_N and RoeM_N schemes are validated by six test cases showing various aspects of multiphase flow physics. The performances of AUSMPW+_N and RoeM_N are compared with those of the Roe's flux difference splitting (FDS) [28], preconditioned Roe's FDS (p-Roe) [22], and AUSM$^+$-up schemes. Section 4.1 is computed with an explicit Euler method and first-order flux schemes. Elsewhere, unsteady calculations are performed by the third-order total-variation-diminishing (TVD) Runge–Kutta scheme [29], and steady-state calculations are performed by the preconditioned lower–upper symmetric Gauss–Seidel (LU-SGS) method [30]. The MLP5 limiter [31] is employed to obtain accurate monotonic solutions. The turbulent problems in Sects. 4.5 and 4.6 are solved by the $k-\omega$ SST turbulence model.

Table 1 summarizes the basic flow characteristics and the primary rationale for each validation problem.

4.1 Quirk's test

The Quirk's odd–even decoupling test [32] is well known for examining the basic shock stability characteristics of a numerical scheme. A plane moving shock wave with $M_{\mathrm{s}} = 6$ is simulated with a grid perturbed along the centerline. Whereas the AUSMPW+ and RoeM schemes in gas dynamics are known to be stable in this test, Roe's FDS suffers from a carbuncle phenomenon [24,25]. We conduct the same

Table 1 Summary of validation problems (liq: liquid, vap: gas phase of the same fluid, gas: non-condensable gas)

Sections	Flow regime	Convective flux	EOS	Validation rationale
4.1, 4.2, 4.4	High Mach, unsteady	AUSMPW+_N, RoeM_N, Roe (except Sect. 4.2)	Liq (water): stiffened EOS Gas (air): ideal gas law	Robustness of AUSMPW+_N and RoeM_N in multiphase shock problems
4.3	Low Mach, steady	AUSMPW+_N, RoeM_N, p-Roe, AUSM$^+$-up	Liq (water): stiffened EOS Gas (air): ideal gas law	Accuracy and convergence in low-Mach-number flow
4.5	All Mach, steady	AUSMPW+_N, RoeM_N	Liq, vap (N_2): SBTL from NIST	Accuracy in cryogenic cavitating flow
4.6	High Mach, steady	AUSMPW+_N, RoeM_N, Roe, AUSM$^+$-up	Liq, vap (water): IAPWS97	Accuracy of flux schemes with nucleation model in phase change process

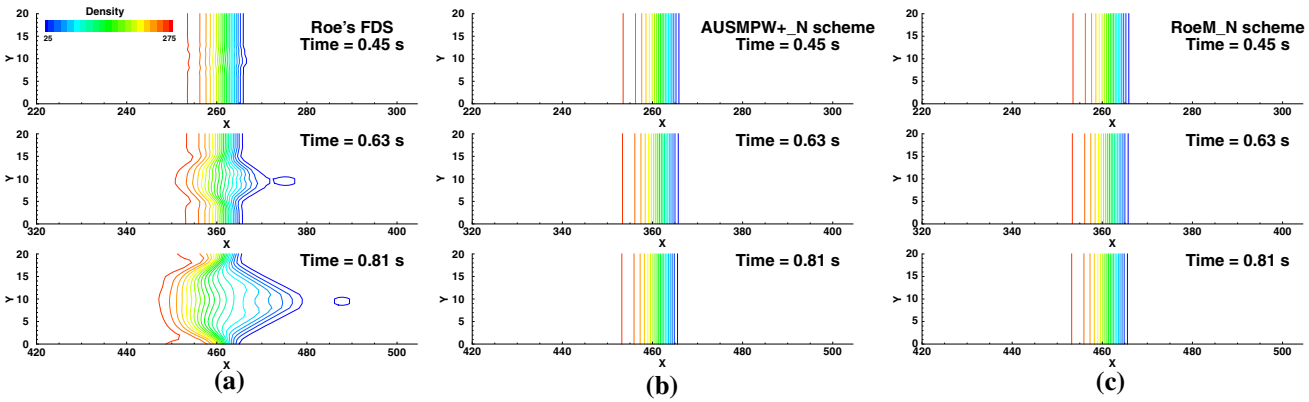

Fig. 3 Density contours in Quirk's test ($y_g = 0.1$). **a** Roe's FDS. **b** AUSMPW+_N. **c** RoeM_N

test in two-phase mixture flows in order to confirm that the same robustness of AUSMPW+ and RoeM is preserved in their multiphase extensions, AUSMPW+_N and RoeM_N schemes. We set $\Delta t = 1 \times 10^{-5}$ s. A uniform, unit-spacing grid of 800×20 cells has the centerline perturbation as follows:

$$y_{i,j_{\mathrm{mid}}} = \begin{cases} y_{j_{\mathrm{mid}}} + 10^{-4}, & \text{for } i \text{ even}, \\ y_{j_{\mathrm{mid}}} - 10^{-4}, & \text{for } i \text{ odd}. \end{cases}$$

Figure 3 shows the results for $y_g = 0.1$. As observed in gas dynamics ($y_g = 1.0$), the Roe's FDS destroys the original planar shock profile by amplifying the numerical error as the shock propagates. Both AUSMPW+_N and RoeM_N capture the monotonic shock profile and remain stable throughout the simulation. Table 2 summarizes the results of Quirk's test for a range of gas mass fractions. The Roe's FDS becomes stable as the two-phase mixture approaches a pure liquid. This result is attributed to the fact that the mixture density is great enough not to be disturbed by the pressure field. Both AUSMPW+_N and RoeM_N are stable at any mass fraction, confirming their robustness in two-phase flows.

Table 2 Results of Quirk's test for various y_g

Gas mass fraction (y_g)	Roe	AUSMPW+_N	RoeM_N
1.0 (gas)	Unstable	Stable	Stable
1.0×10^{-1}	Unstable	Stable	Stable
1.0×10^{-2}	Unstable	Stable	Stable
1.0×10^{-3}	Stable	Stable	Stable
1.0×10^{-4}	Stable	Stable	Stable
1.0×10^{-5}	Stable	Stable	Stable
1.0×10^{-6}	Stable	Stable	Stable
1.0×10^{-7}	Stable	Stable	Stable
1.0×10^{-8}	Stable	Stable	Stable
0.0 (water)	Stable	Stable	Stable

4.2 Two-phase shock-tube

In order to examine the capability to handle stiff problems, two-phase shock-tube test cases are considered. Air and water are initially separated, and water is driven by air according to the initial conditions that are the same as in Ref. [33]. The opposite case at which air is driven by water is also computed with the initial condition in the same reference

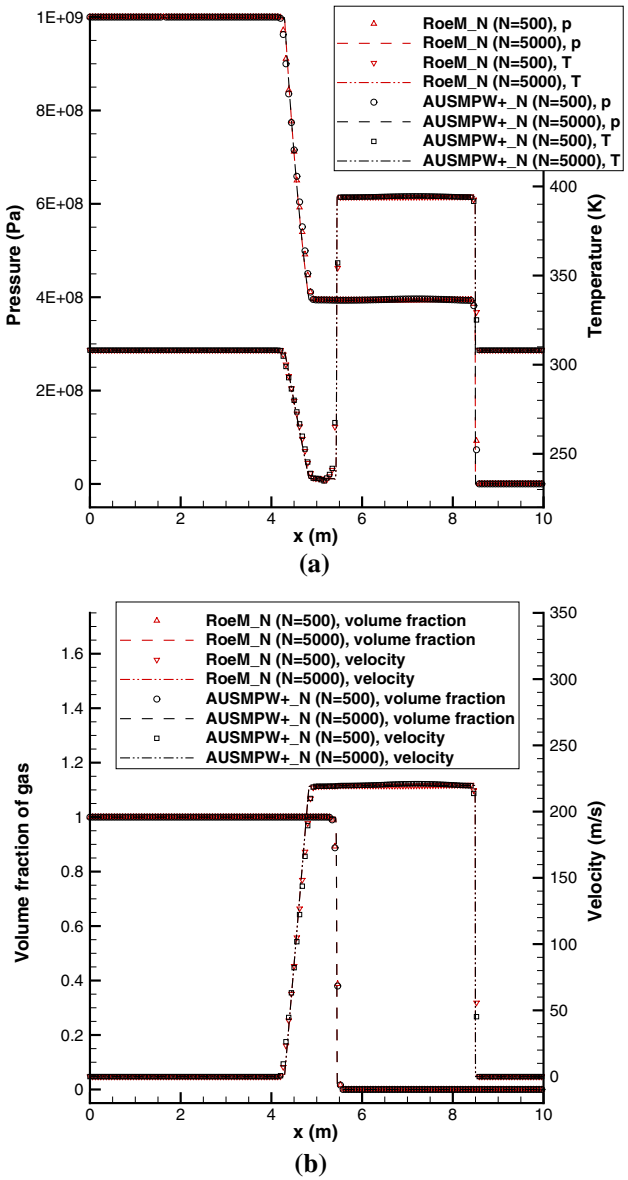

Fig. 4 Solutions of air-to-water shock-tube problem at $t = 2$ ms. **a** Pressure and temperature distribution. **b** Volume fraction and velocity distribution

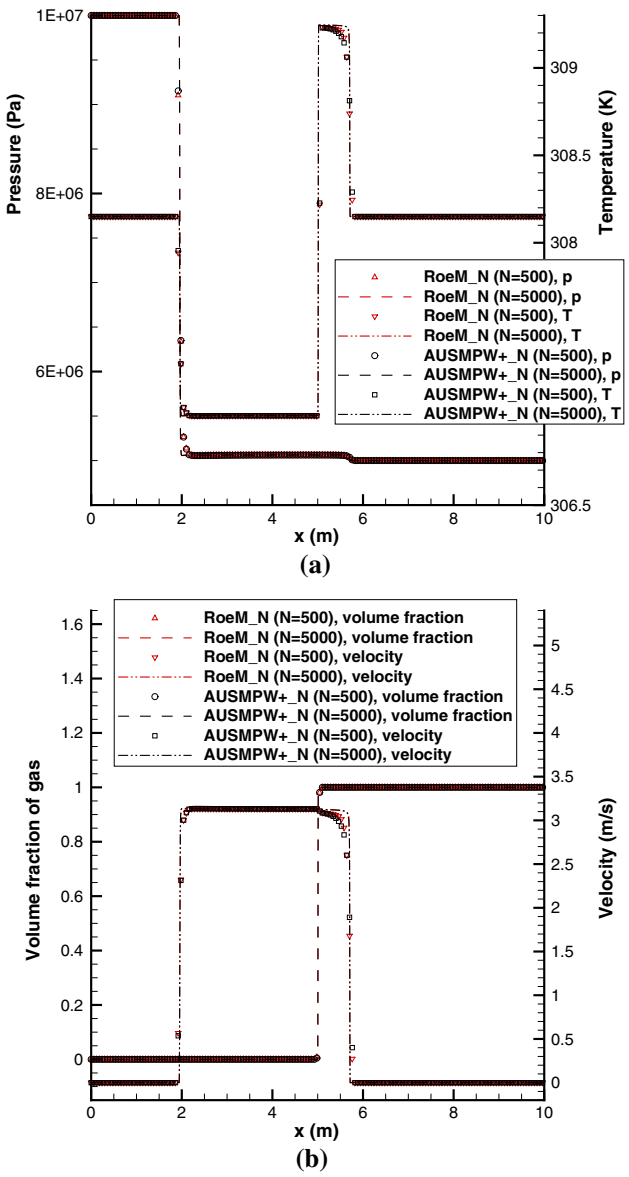

Fig. 5 Solutions of water-to-air shock-tube problem at $t = 2$ ms. **a** Pressure and temperature distribution. **b** Volume fraction and velocity distribution

paper. Since this test case does not consider the phase change phenomenon, the vapor phase is not included. Each problem is computed up to 2.0×10^{-3} s with $\Delta t = 2.0 \times 10^{-6}$ s for $N = 500$ grid (CFL ≈ 0.2).

To demonstrate grid convergence, additional computations are carried out on $N = 2500$ and 5000 grids. For the purpose of brevity and avoiding untidiness, the results with $N = 500$ and 5000 are presented. Figures 4 and 5 show the profiles of the velocity, pressure, temperature, and volume fraction for the air-to-water and water-to-air shock-tube problems, respectively. The solution of $N = 500$ grid is plotted for every third point for clarity. All flow features including shock waves, rarefaction waves, and phase interface are resolved sharply, and the computed solutions remain stable as the grid system is refined. In the case of the air-to-water shock-tube, a strong shock is transmitted into the liquid phase and rarefaction waves are reflected back into the air phase. In the other case, a shock is transmitted into the gas phase and rarefaction waves are reflected back into the liquid phase.

4.3 Inviscid mixture flow around a cylinder

As a test of checkerboard instability at low-Mach-number flows, an air–water mixture flow around a cylinder is solved. The computations are performed on a 72×100 O-type grid. The initial gas volume fraction is set to 0.1. The free stream

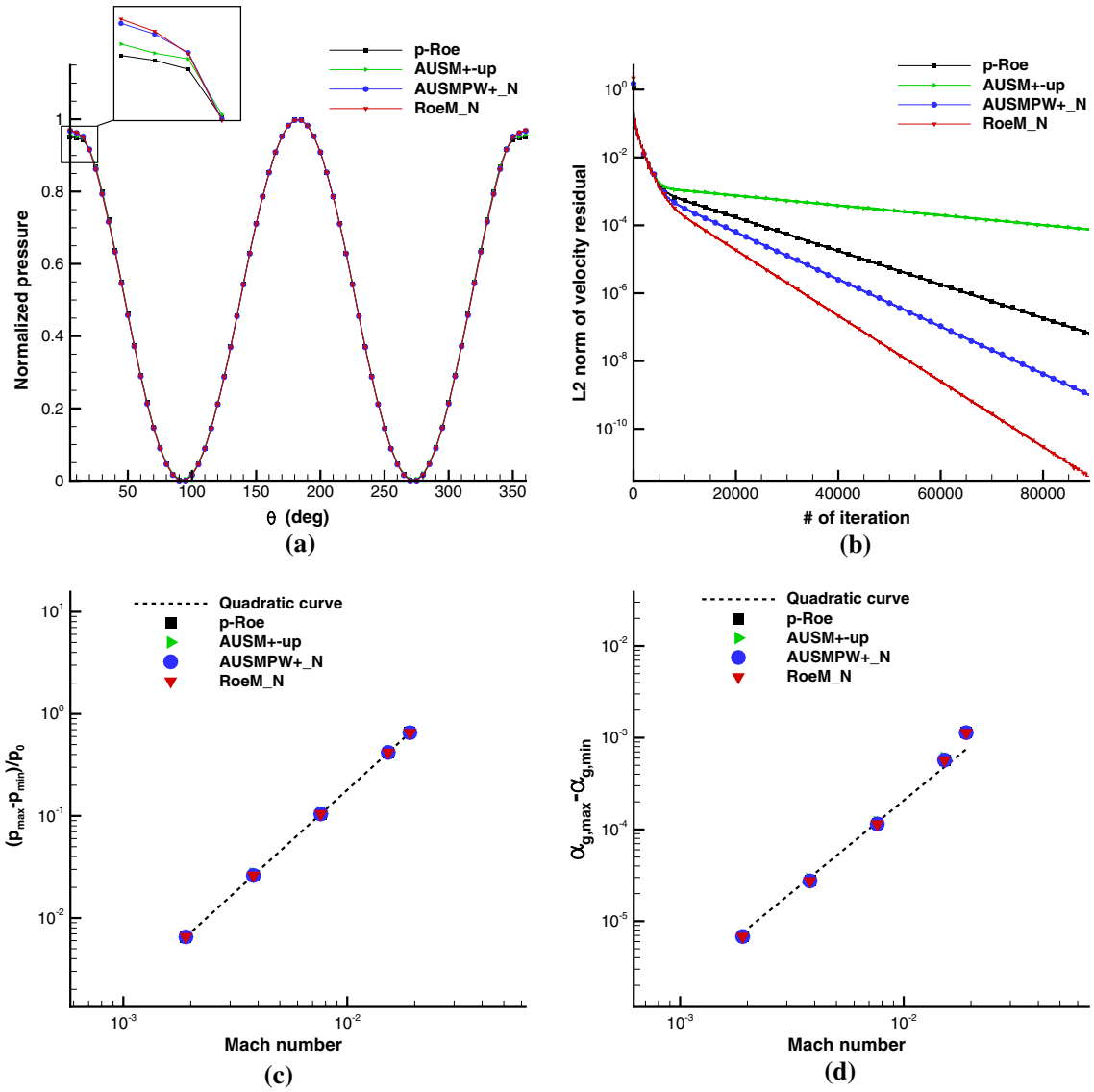

Fig. 6 Results of mixture flow around a cylinder. **a** Pressure over a cylinder surface ($V_\infty = 0.5$ m/s). **b** Convergence history ($V_\infty = 0.5$ m/s). **c** Fluctuation of static pressure. **d** Fluctuation of gas volume fraction

velocities are varied as $V_\infty = 0.5,\ 1,\ 2,\ 4,\ 5$ m/s at $P_\infty = 101{,}325$ Pa, $T_\infty = 300$ K, so the free stream Mach number ranges roughly from 2×10^{-3} to 2×10^{-2}. For the purpose of comparison, we solve the same problem with the p-Roe and AUSM$^+$-up schemes which are known to perform successfully in steady low-Mach-number flows.

Figure 6a plots the normalized pressure distribution along the cylinder surface when $V_\infty = 0.5$ m/s. The curves are smooth, indicating the absence of numerical instabilities. AUSMPW+_N and RoeM_N produce slightly more accurate solutions than p-Roe and AUSM$^+$-up at the rear stagnation point ($\theta = 0°,\ 360°$). The convergence behaviors are plotted in Fig. 6b, showing that the residual decreases faster in RoeM_N and AUSMPW+_N. Figure 6c, d displays log–log plots of the pressure fluctuation ($\equiv (p_{\max} - p_{\min})/p_\infty$) and the fluctuation of the gas volume fraction ($\equiv (\alpha_{g,\max} - \alpha_{g,\min})$) in terms of the inflow Mach number. As the spatial pressure distribution is related to the p_2 field [34] in the low-Mach-number limit, the pressure fluctuation should exactly scale with M_∞^2 . The proposed schemes match the theoretical asymptotic prediction, and the fluctuation of the gas volume fraction also scales with M_∞^2 as seen in the low-Mach-number two-phase channel flows in Ref. [35].

4.4 Inviscid interaction between a shock and a water column

Next, we demonstrate the capability of the proposed schemes in intricate compressible two-phase flows. We model the interaction between a shock in air and a water column (i.e., a

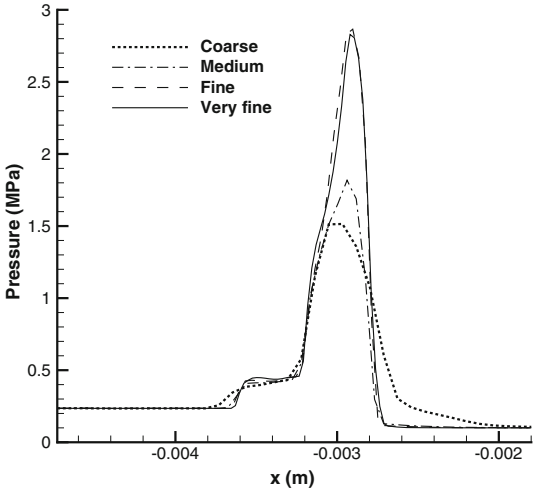

Fig. 7 Grid convergence study for the interaction between a shock and a water column: centerline pressure at $t = 3.0\ \mu$s

2-D droplet). A cylindrical water column of diameter 6.4 mm centered at the origin is struck by a moving air shock of $M_s = 1.47$.

The grid convergence study is conducted using four different grids. The fine grid is uniformly refined to $\Delta x = \Delta y = 0.025$ mm near the water column ($[-5\,\text{mm}, 5\,\text{mm}]\times[-5\,\text{mm}, 5\,\text{mm}]$), and it stretches outward to cover the whole domain ($[-15\,\text{mm}, 20\,\text{mm}]\times[-15\,\text{mm}, 15\,\text{mm}]$) with 900×840 cells. Similarly, the coarse/medium/very fine grids are generated, respectively, using 450×420, 675×630, 1350×1260 cells. Figure 7 shows the centerline pressure near the water column after the impact of shock at $t = 3.0\ \mu$s. As the fine and very fine grids yield the almost similar pressure peaks inside the water column, the fine grid is used throughout computations. The initial conditions are those in Ref. [33].

$$
\begin{aligned}
\mathbf{Q}_L &= (235438\ \text{Pa}, 225.86\ \text{m/s}, 0\ \text{m/s}, 381.85\ \text{K}, 0, \varepsilon_{1\text{L}}) \\
&\quad x \le -4\ \text{mm}, \\
\mathbf{Q}_\text{R} &= \left(1\times10^5\ \text{Pa}, 0\ \text{m/s}, 0\ \text{m/s}, 293.15\ \text{K}, 0, \varepsilon_{1\text{R}}\right) \\
&\quad x > -4\ \text{mm}, \\
\mathbf{Q}_\text{droplet} &= \left(1\times10^5\ \text{Pa}, 0\ \text{m/s}, 0\ \text{m/s}, 293.15\ \text{K}, 0, \varepsilon_2\right) \\
&\quad R < 3.2\ \text{mm}.
\end{aligned}
$$

Here, $\varepsilon_{1\text{L}} = 0.99616269796$, $\varepsilon_{1\text{R}} = 0.99101366252$, and $\varepsilon_2 = 1.10282248889\times10^{-8}$ are the gas mass fractions corresponding to the gas volume fractions of 0.99999 and 1×10^{-5}, respectively. At the water column interface, a transition region with a width of $\pm2\Delta x_\text{min}$ is specified by the blending function, which imposes a smooth change in the gas volume fraction across the phase interface. Computations are then executed up to 96 μs with $\Delta t = 2\times10^{-9}$ s (CFL ≈ 0.3).

The pressure evolution during the early stage is presented in Fig. 8. When the incident shock hits the water column, it splits into a reflected shock which retracts and a transmitted shock which accelerates inside the water column. At the rear end of the water column, the transmitted shock reflects as expansion waves (Fig. 8b). The waves inside the water column constantly propagate back and forth and interact with one another, forming a complex flow structure (Fig. 8c). Both the AUSMPW+_N and RoeM_N schemes successfully capture the detailed wave patterns. In particular, the shock-discontinuity-sensing term (52) detects the two-phase shock discontinuity without confusing it with the phase interface. Note that Roe's FDS is unable to compute this problem. At a later stage, the water column is deformed and a Richtmyer–Meshkov instability is observed (Fig. 8d).

Furthermore, the effect of an EOS on the solution behavior across a contact discontinuity is examined. It is known that spurious pressure oscillations across a contact discontinuity (or a phase interface) may appear in the conservative form of finite volume discretization. When a contact discontinuity is away from a cell-interface, the cell-averaged pressure, which is obtained via the EOS with the cell-averaged density, specific energy, and mass fraction, conforms to the physical pressure at a contact discontinuity only when the EOS is linear. If there are two different EOSs across a contact discontinuity within a computational cell, oscillations are in general unavoidable due to the finite volume cell average process.

In this test case, even if each EOS for the liquid and gas phase is linear (say, the ideal gas EOS for the gas phase, and the stiffened gas model for the liquid phase), the combined EOS for the mixture at the phase interface is not linear. As shown in Fig. 9, however, the computed results do not seem to show any noticeable oscillations across the phase interface. If we change the EOS for water with the SRK (Soave–Redlich–Kwong) EOS [36], a nonlinear cubic EOS, weak wiggles are visible near the left phase interface as in Fig. 10. Research to cure this behavior have been carried out by many researchers, but each is limited to its target EOS formulation [37–39]. At the same time, however, it should be noted that incorrect wave speeds and pressure wiggles inside the water column in Fig. 10 partly arise from inaccurate prediction of liquid properties by the SRK EOS, indicating that the choice of an EOS suitable to the problems of interests is important. As shown in Fig. 9, if an EOS for each phase gives physically reasonable fluid properties for the problem, and if the combined EOS behaves almost linearly within a computational cell, the major flow features do not seem to be impeded by the spurious oscillations.

4.5 Cryogenic cavitating turbulent flow around a hydrofoil

To validate the proposed methods in flows with real fluids, we simulate Hord's experiments [40] of cryogenic cavitating flows around a hydrofoil. The widths of the tunnel and

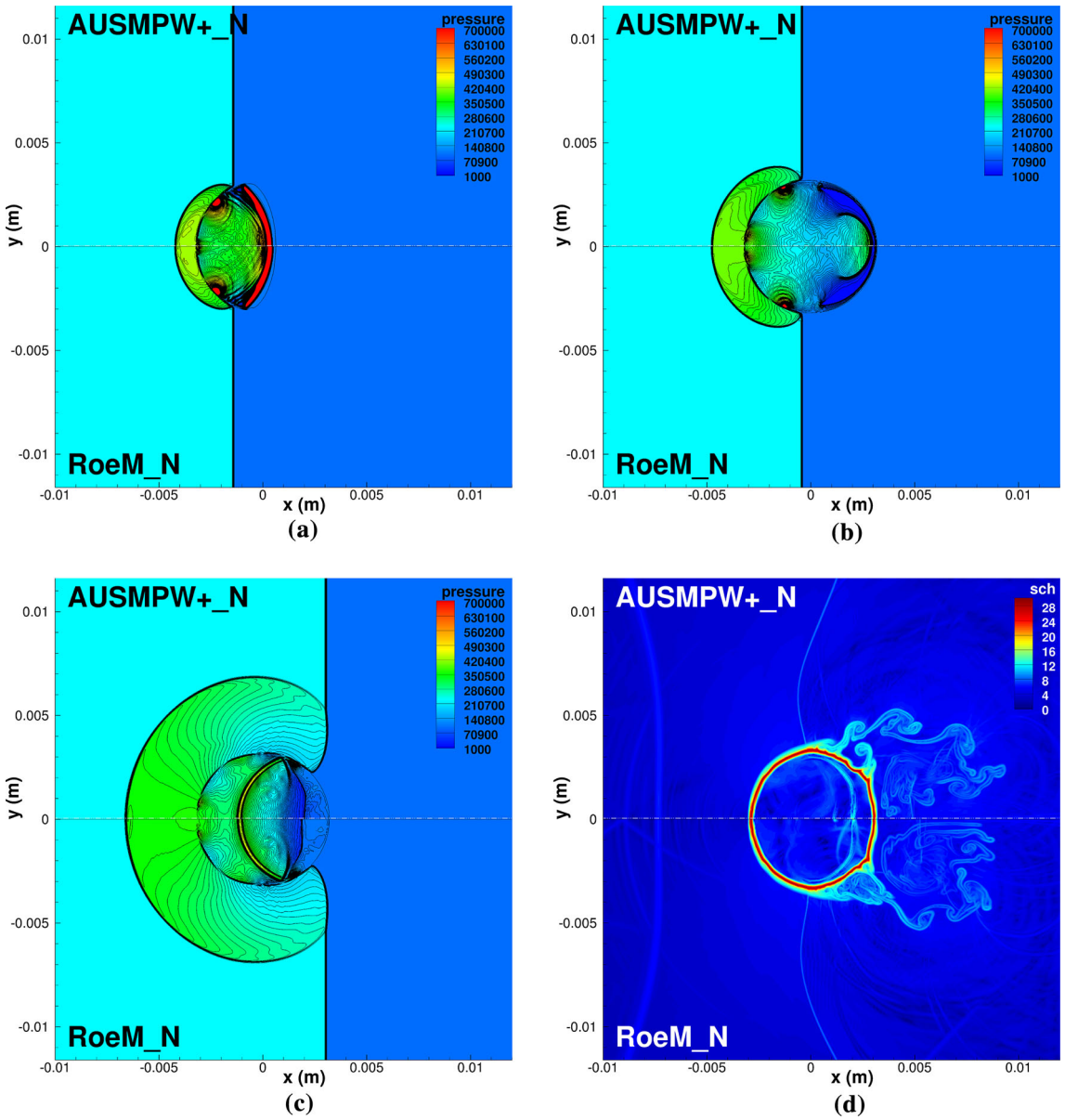

Fig. 8 Time evolution of interaction between an air shock and a water column. **a** Pressure contour at $t = 5.2$ μs. **b** Pressure contour at $t = 7.2$ μs. **c** Pressure contour at $t = 14.2$ μs. **d** Numerical schlieren at $t = 96$ μs

hydrofoil are 25.4 and 7.92 mm, respectively. The computational domain is shown in Fig. 11. The whole flow field is divided into over 51,500 cells, and the grid near the hydrofoil wall is refined to emulate the wall effect. The value of y^+ along the hydrofoil wall is approximately 1. The mass flux and free stream temperature are imposed at the tunnel inlet. At the tunnel outlet, the pressure outlet boundary condition is used. The CFL number is set to 5. Among various test cases, we calculate run number 289C in which the working fluid is liquid nitrogen under the free stream conditions $T_\infty = 88.64$ K, $V_\infty = 23.5$ m/s, and the cavitation number $\sigma_\infty = 1.55$. The phase change is taken into account by the Schnerr–Sauer cavitation model.

Figure 12 presents the numerical results of the AUSMPW+_N and RoeM_N schemes. As shown in Fig. 12b, a locally supersonic flow region exists in the cavity, while the entire flow field outside the cavity is incompressible. This demonstrates the effectiveness of AUSMPW+_N and RoeM_N in dealing with two-phase real-fluid flows spanning from subsonic to supersonic Mach numbers. Figure 13 quantitatively compares the computed surface pressure depression $(p - p_{\text{sat},\infty})$ and temperature results with experiment and another computation [7,40]. The pressure depression in Fig. 13a reveals the thermal effect of the cryogenic cavitating flows. A working fluid with negligible thermal effect (such as water) would yield a minimum pressure depres-

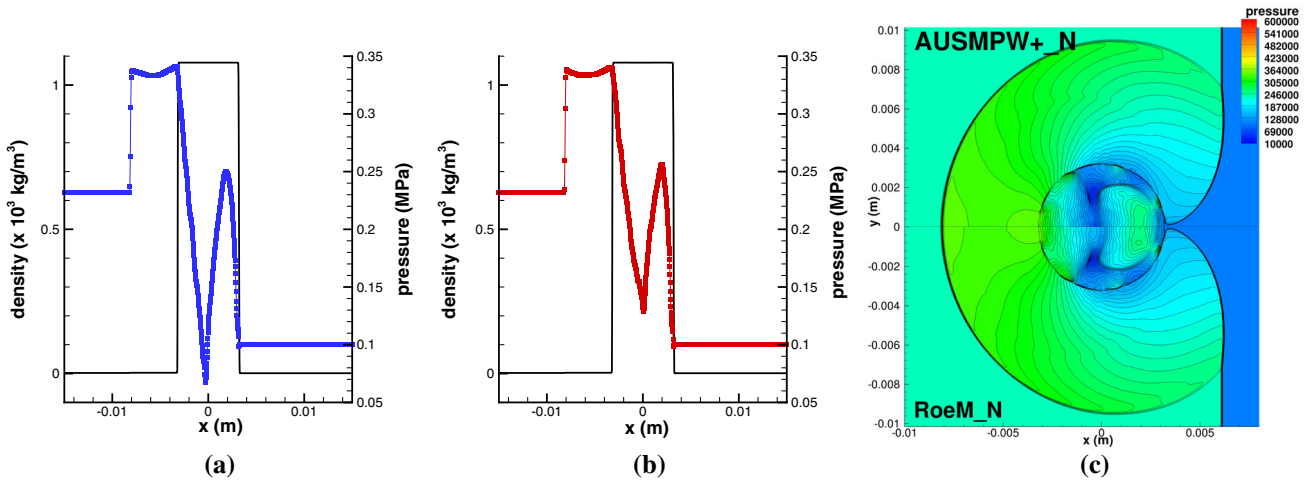

Fig. 9 Centerline plots (black solid line: density; color symbols: pressure) and pressure distribution at $t = 20.4$ μs (stiffened gas EOS for water). **a** AUSMPW+_N. **b** RoeM_N. **c** Pressure distribution

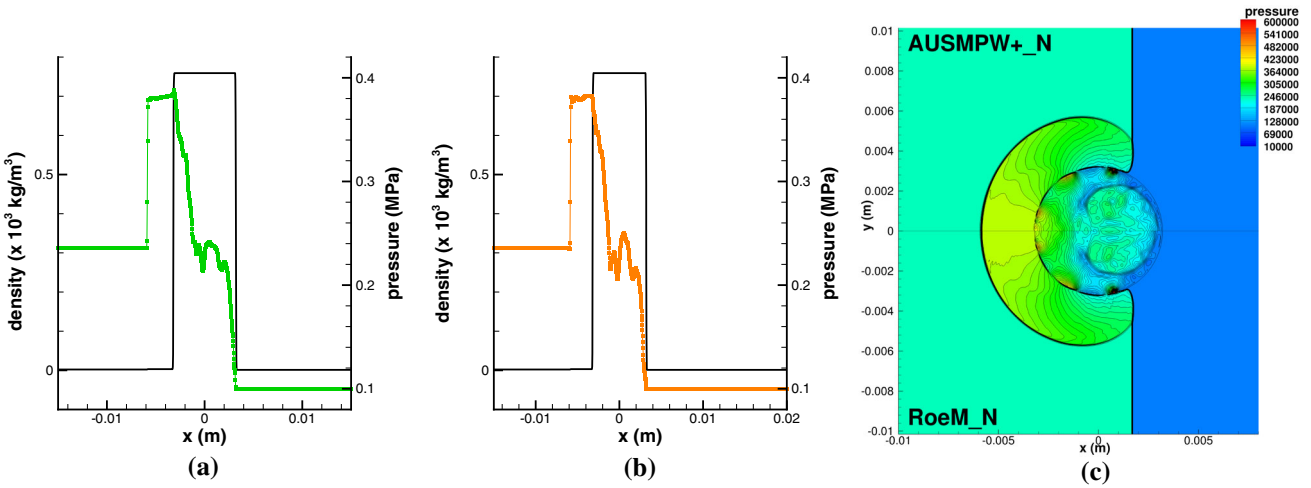

Fig. 10 Centerline plots (black solid line: density; color symbols: pressure) and pressure distribution at $t = 11.4$ μs (SRK EOS for water). **a** AUSMPW+_N. **b** RoeM_N. **c** Pressure distribution

sion of zero. In cryogenic fluids, the thermal effect decreases the local temperature, and hence the local vaporization pressure. Consequently, a negative pressure depression appears in Fig. 13a.

4.6 Steam-condensing turbulent flow in a nozzle

Two-phase steam-condensing problems are chosen to examine the capability to handle non-equilibrium phase change flows of water and steam. We simulate the nozzle B and nozzle C cases in the 2-D experiments of Moore et al. [41]. The computational domain is shown in Fig. 14. Cases B and C are simulated on 180×70- and 150×70-sized grids, respectively. The total pressure and temperature of the subsonic flows at the nozzle inlets are summarized in Table 3. At the nozzle outlet, a supersonic outlet boundary condition is applied. We adopt the nucleation-theory-based model to capture the phase change phenomenon.

Figure 15 compares the computed and experimental pressures along the nozzle centerlines. The computational predictions obtained by AUSMPW+_N and RoeM_N excellently agree with experimental results in both cases. The pressure rise downstream of the nozzle throat behaves similarly to an aerodynamic shock and is often called a condensation shock as it occurs during phase change. Unlike an aerodynamic shock in which the post-shock condition is usually subsonic, the post-shock condition of a condensation shock is sonic at most. Since this test case deals with a fully compressible mixture flow without strong shock or phase interfaces, the results of Roe and AUSM$^+$-up are quite similar. Figure 16 compares the computed droplet radius along the axial distance with another computational result [42] and experimental data

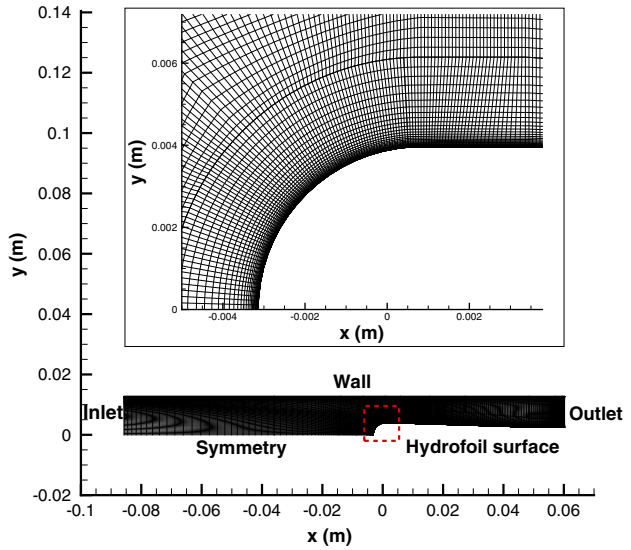

Fig. 11 Computational domain and grid distribution for cryogenic cavitating flow around a hydrofoil

measured at the nozzle outlet [41]. Judging from the uncertainty in measurement at this scale [42], the computational prediction is quite acceptable. This problem is a typical non-equilibrium phase change phenomenon, so employing the nucleation-theory-based model is essential.

5 Applications

In Sect. 4, the multiphase solver with the proposed numerical schemes and physical models was validated by various inviscid/turbulent test problems. The multiphase solver is applicable to a broad spectrum of multiphase phenomena. This section focuses on realistic applications with turbulent multiphase flows.

5.1 Flow inside a thermal vapor compressor

The thermal vapor compressor (TVC) improves the efficiency of thermal desalination plants by recycling the vaporized steam. Figure 17 is the schematic of a TVC system. The desalination process releases steam at low pressure and temperature, which is entrained into the TVC through the suction nozzle (called the suction steam). The suction steam is then entrained and repressurized by mixing with the primary steam at high pressure and temperature. Therefore, the suction performance of a TVC is generally evaluated by the entrainment ratio (ER), defined as the mass flow rate ratio between the suction and the primary nozzle.

For the droplet-condensing flow inside a thermal vapor compressor, surrounding steam vapor and the small liquid droplets generated can be regarded as a carrier phase and

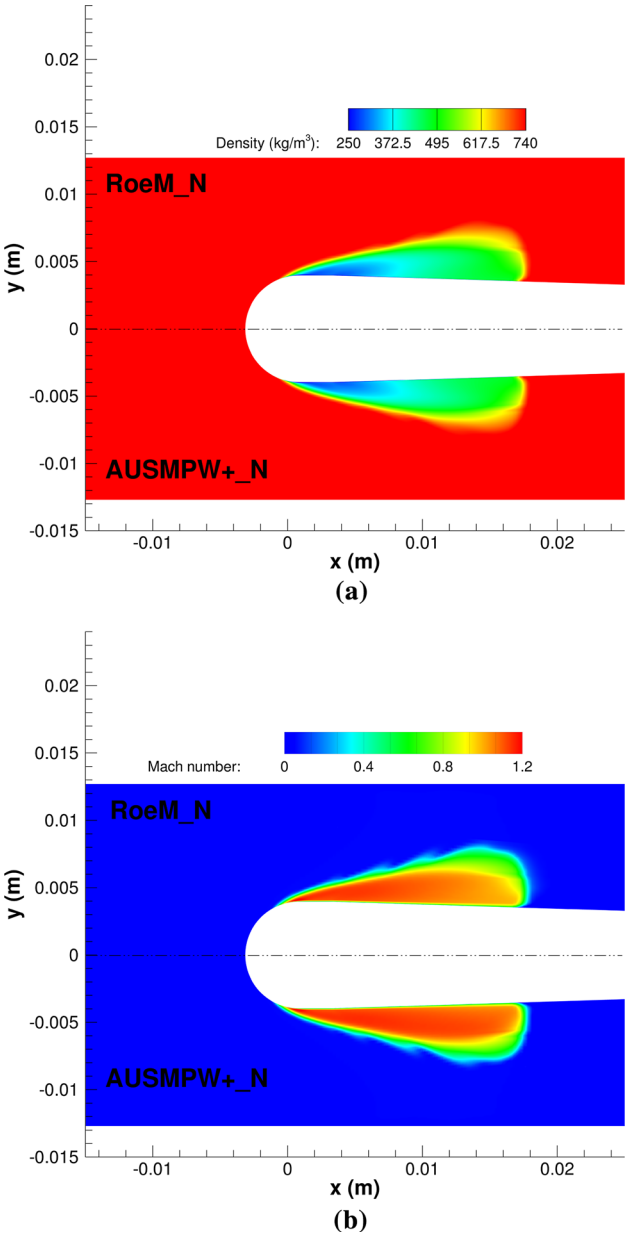

Fig. 12 Numerical results of cryogenic cavitating flow around a hydrofoil. **a** Density contour. **b** Mach number contour

suspended particles, respectively. In that case, the velocity difference between phases is hardly substantial, and thus, the assumption of the velocity equilibrium is acceptable. Since the droplet size is very small, the temperature equilibrium is also acquired. Within the homogeneous mixture framework, a robust and accurate numerical scheme is essential when computing flows inside a TVC. Roe's FDS turns out to be unsuitable for TVC computations, because it often fails in computations due to the shock instability and positivity problems. On the contrary, both AUSMPW+_N and RoeM_N produce stable and accurate results (see Fig. 18).

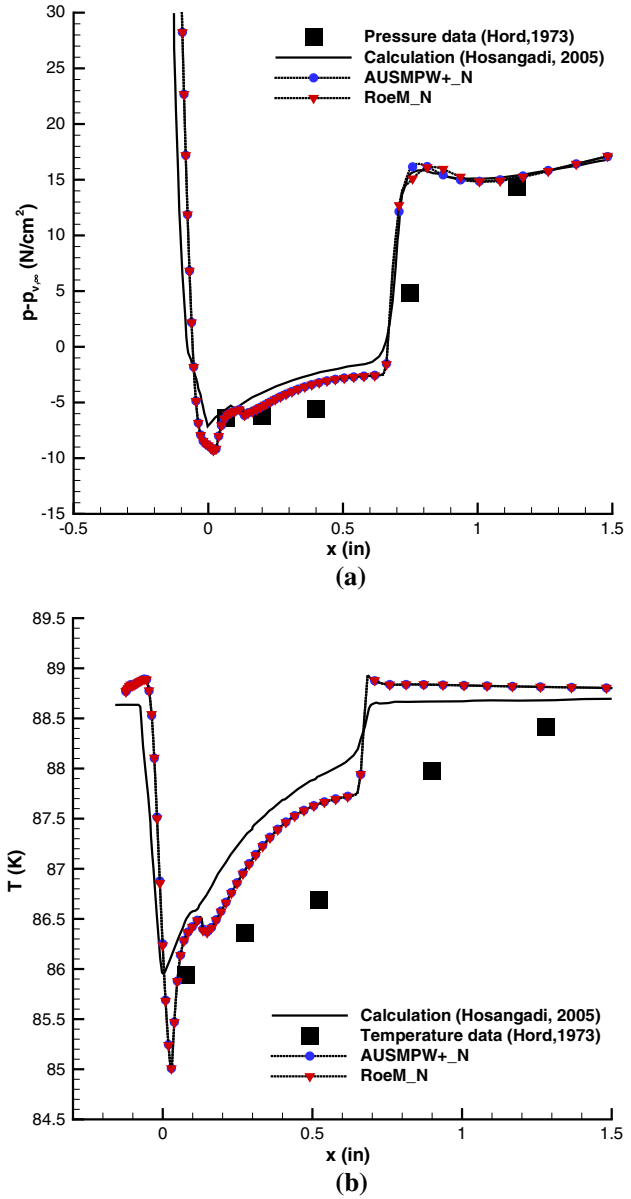

Fig. 13 Comparison of surface pressure depression and temperature distribution. **a** Surface pressure depression. **b** Surface temperature

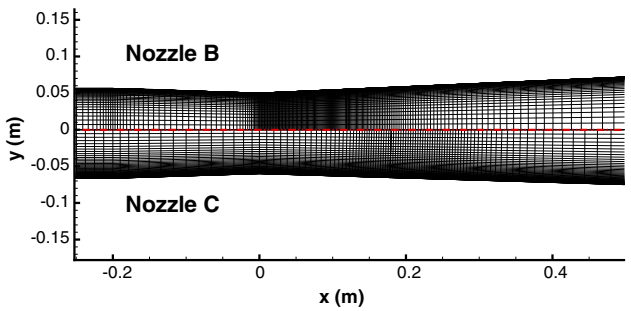

Fig. 14 Computational domains and grid distributions of steam-condensing flow in the Moore nozzles (cases B and C)

Table 3 Inlet boundary conditions for steam condensing flow in a nozzle

	Inlet total pressure (Pa)	Inlet total temperature (K)
Moore B	25,000	357.6
Moore C	25,000	358.6

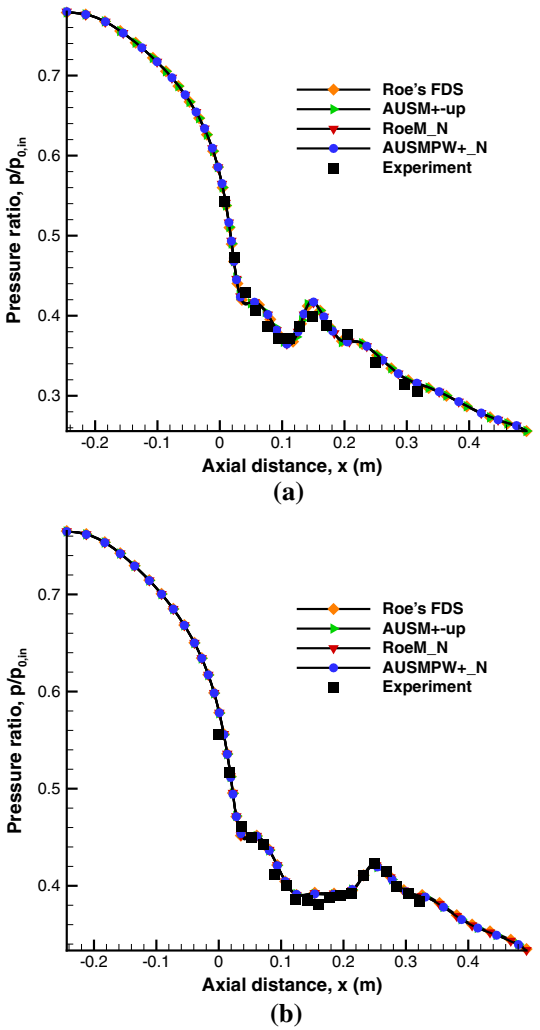

Fig. 15 Comparison of computed and experimental pressure distributions along the centerlines for steam-condensing flow in a nozzle. **a** Nozzle B. **b** Nozzle C

The modeling of the phase change process is also important, because liquid droplets form and decay depending on the position of the shock and expansion fan in the shock-train region. To accommodate such flow physics, we adopt the nucleation-theory-based model and the Hertz–Knudsen-equation-based model. The accommodation coefficients in the Hertz–Knudsen-equation-based model are set to 0.1. The properties of the working fluid, steam and water, are evaluated by the IAPWS97 formulation. The LU-SGS method is adopted for an efficient time integration, and the turbulence

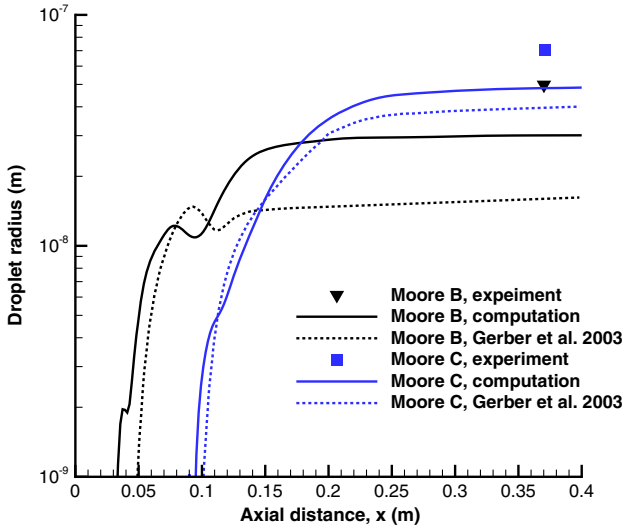

Fig. 16 Comparison of computed and experimental measures of droplet size along the centerline

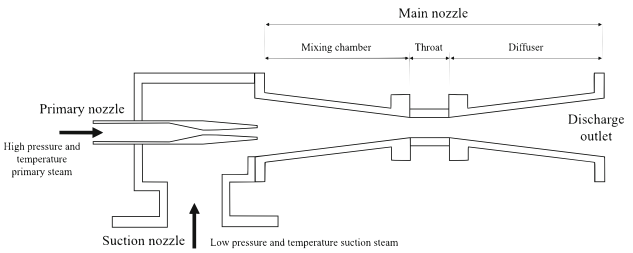

Fig. 17 Schematic of a TVC system

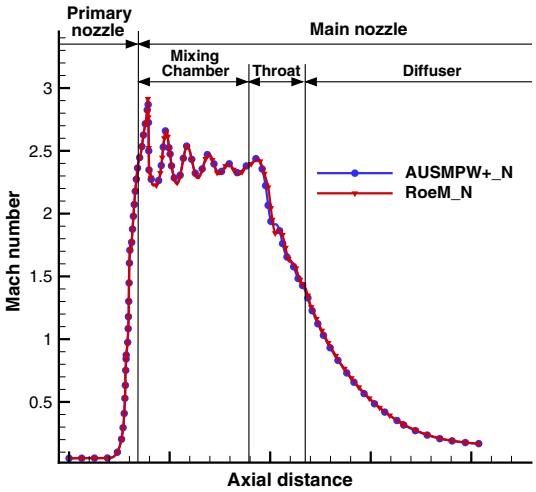

Fig. 18 Comparison of computed Mach number distributions along the centerline for TVC configuration #2

effects are taken into account by the $k-\omega$ SST model. The target TVCs are experimentally tested by Doosan Heavy Industries, and their flow conditions are summarized in Table 4. The compression ratio in Table 4 is defined as the pressure ratio between the discharge outlet and the suction steam.

Table 4 Operating conditions for TVC

Configuration	Primary pressure (bar)	Compression ratio
#1	2.5	1.796
#2	3.4	1.8
#3	5.968	2.437
#4	9.6	1.853
#5	13.3	1.936

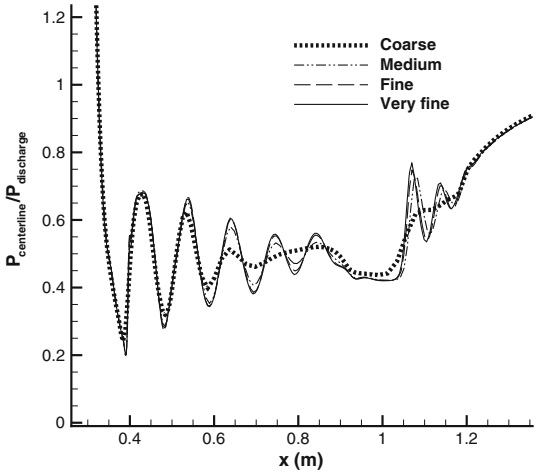

Fig. 19 Grid convergence study for TVC: pressure fluctuation around shock-train region

To demonstrate the grid convergence behavior, computations are carried out for configuration #2 by changing the number of cells in four different grids. Figure 19 shows the centerline pressure fluctuation. Since the results of the fine and very fine grids are almost indistinguishable, the fine grid is used throughout the computations.

5.1.1 Phase change phenomena and ER

Table 5 compares the computed ER in single- and two-phase computations. Note that the values of ER and mass flow rate in Table 5 are normalized by the experimental data. The entrainment ratio error (ER error) denotes the percent deviation between computed and experimentally measured ER values as follows:

$$\text{ER error} = \left| \frac{\text{ER}_{\text{experimental}} - \text{ER}_{\text{computed}}}{\text{ER}_{\text{experimental}}} \right| \times 100\,(\%)\,.$$

Two-phase computations provide a remarkable improvement over single-phase computations which yield substantially incorrect results in several configurations.

Two-phase computations consider the latent heat during the phase change process which is ignored in single-phase computations. If phase change is excluded, the thermodynamic energy reduction by the flow expansion is completely

Table 5 Comparison of entrainment ratios of phase change models in TVC

Configuration	Computational approach	Primary mass flow rate	Suction mass flow rate	Entrainment ratio	Entrainment ratio error (%)
#1	Single-phase	1.017	0.538	0.529	47.1
	Two-phase (nucleation)	1.017	0.922	0.906	9.40
	Two-phase (Hertz–Knudsen)	0.978	0.910	0.930	7.00
#2	Single-phase	1.022	0.544	0.532	46.8
	Two-phase (nucleation)	0.995	0.973	0.978	2.15
	Two-phase (Hertz–Knudsen)	0.985	0.958	0.972	2.76
#3	Single-phase	0.931	0.974	1.047	4.67
	Two-phase (nucleation)	0.945	0.991	1.048	4.84
	Two-phase (Hertz–Knudsen)	0.921	0.986	1.070	7.02
#4	Single-phase	0.972	0.904	0.930	7.03
	Two-phase (nucleation)	0.975	0.942	0.967	3.34
	Two-phase (Hertz–Knudsen)	0.954	0.934	0.980	2.02
#5	Single-phase	0.995	0.379	0.381	61.9
	Two-phase (nucleation)	1.009	0.952	0.943	5.68
	Two-phase (Hertz–Knudsen)	0.982	0.951	0.968	3.19

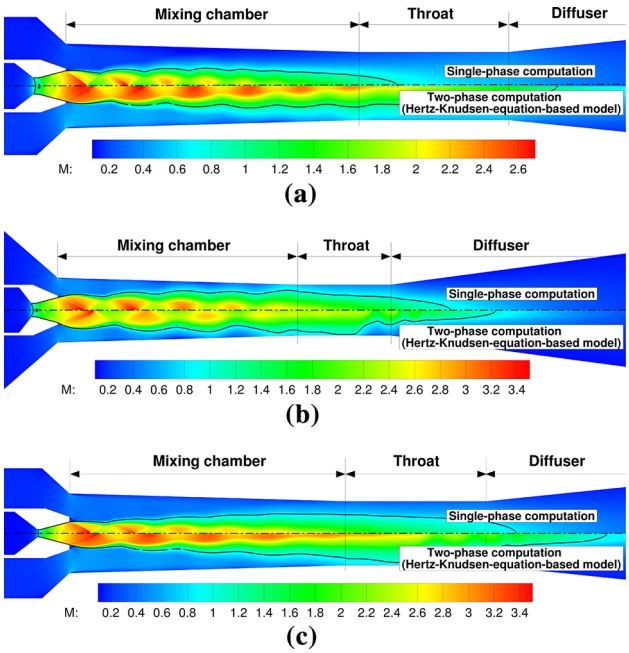

Fig. 20 Comparison of Mach number contours in single- and two-phase flow computations. **a** Configuration #1. **b** Configuration #3. **c** Configuration #4

converted into the kinetic energy. Conversely, if phase change is considered, a portion of this thermodynamic energy is released as the latent heat during condensation, and only the remnant converts into the kinetic energy. Meanwhile, across the shock, a portion of the kinetic energy is absorbed by vaporization. Owing to this latent heat exchange, the compressible waves tend to be weaker in two-phase computations than in single-phase computations. The results of single- and

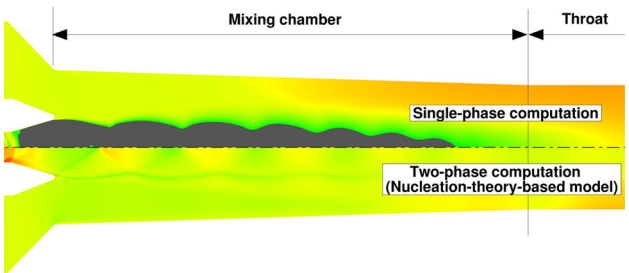

Fig. 21 Comparison of temperature distributions of configuration #1, computed by the single- and two-phase flow models

two-phase computations compared in Fig. 20 confirm that the Mach number contours vary more vigorously in single-phase than in two-phase computations.

Figure 21 compares the temperature distributions of single- and two-phase computations. The gray-marked area in Fig. 21 indicates the region that the local temperature is below the triple point of water (273.16 K). Although the local temperature is decreased by flow expansion, it does not fall below the triple point. Two-phase computations are consistent with this physical constraint because the strength of the expansion fan is weakened by the latent heat exchange. On the contrary, a single-phase computation yields unphysical results around the shock-train region.

Single-phase computations fail to replicate the flow physics in the shock-train region, but the ER unexpectedly matches well the experimental measurements in configurations #3 and #4 (see Table 5). The reason for these results is clarified in Fig. 20, which compares configurations #3 and #4 with configuration #1. The black solid line in Fig. 20 represents the sonic line. We observe that single-phase com-

putations reduce the shock-train region in all configurations. This does not produce a noticeable error in configurations #3 and #4 because the main nozzle is choked despite the shortened shock-train region. In configuration #1, however, the choking condition is not achieved with the shortened shock-train, while the choked flow is experimentally observed in all configurations. Since deviation from the choking condition in the main nozzle drastically reduces the ER, the entrainment ratio error becomes enormous in single-phase computation of configuration #1. Thus, we conclude that the modeling of phase change is indispensable for accurate prediction of TVC suction performance, regardless of the flow conditions.

5.1.2 Phase change models and local flow physics

The phase change models based on the nucleation theory and Hertz–Knudsen equation predicts reasonable ER (see Table 5), but the local flow physics differs as shown in Fig. 22.

In the converging part of the primary nozzle, the saturation pressure (which is a function of the local temperature) drops more quickly than the local pressure. Since the Hertz–Knudsen-equation-based model determines the phase change rate by the difference between the local and saturation pressures only, the condensation process starts to occur around the first expanding corner of the primary nozzle throat. On the other hand, the nucleation-theory-based model additionally considers the droplet size and distribution for phase change. Thus, the nucleation-theory-based model yields a delayed onset of the condensation process around the second expanding corner (see Fig. 22a). Due to the liquid phase formed at the nozzle throat in the Hertz–Knudsen-equation-based model, the mixture speed of sound is lowered significantly, and an expansion fan followed by a reflected shock (or a shock-train) is developed (see Fig. 22b). As the reflected shock is very weak, it impinges merely as a compression wave on the wall. Nevertheless, the compression wave increases the local pressure and this pressure increment is propagating to the upstream region through the boundary layer. This pressure increment reduces the Mach number at the primary inlet in the Hertz–Knudsen-equation-based model, because the inlet boundary condition keeps the stagnation properties constant throughout the computations. Reduction in the inlet Mach number eventually decreases the inlet mass flow rate.

The nucleation-theory-based model does not show the aforementioned compressible mechanism around the primary nozzle throat, since the flow is gradually expanded without any compression mechanism. As a result, the primary mass flow rates of the nucleation-theory-based model are larger than those of the Hertz–Knudsen-equation-based model and closer to the experimental data (see Table 5).

For more rigorous comparison, additional experimental data might be necessary such as the local pressure or temperature distributions along the centerline, or the overall

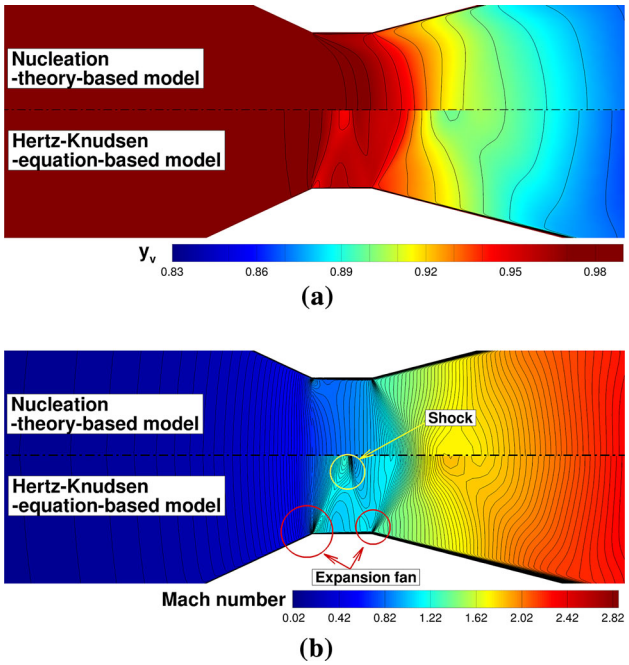

Fig. 22 Comparison of phase change models inside the primary nozzle of configuration #2. **a** Mass fraction. **b** Mach number

ER curve. Nonetheless, the Hertz–Knudsen-equation-based model can be an attractive choice from the viewpoint of computational cost because it does not require the conservation law for the droplet number density in the governing equations.

5.2 Active pressurization in a cryogenic tank

Propellant and oxidizer in the cryogenic tank of a liquid rocket experience varying temperature and pressure from the initial filling process to the end of the flight. The cryogenic tank environment is greatly influenced by heat leakage from the tank wall, change of gravity in the rocket acceleration, injection of the pressurizing agent, and the accompanying phase change. Analyzing the pressure rise and rate of the phase change inside the tank is important for the economic management of cryogenic liquids and the design of the tank system. This section focuses on the active pressurization phase, in which the tank pressure is raised by the injection of the pressurizing agent.

We simulate the E-1 high-pressure LOX tank from NASA Stennis Space Center [43], a spherical 2600-gallon, vacuum-jacketed tank that is pressurized with superheated nitrogen. The initial conditions of the simulations are listed in Table 6. The simulations are run on an axisymmetric grid. The pressurizing agent enters radially through a diffuser at a mass flow rate of 453.64 kg/s. The injected pressurizing agent immediately slows down to a quasi-stationary state due to the sudden expansion at the inlet, which substantially reduces the drag

Table 6 Initial conditions of the active pressurization simulation

	Liquid	Ullage	Pressurant
Initial fill level (%)	90	10	–
Fluid type	O_2 liquid	O_2 vapor	Gas (O_2, N_2)
Temperature (K)	90.18	135.16	288
Pressure (MPa)	2.24	2.24	–

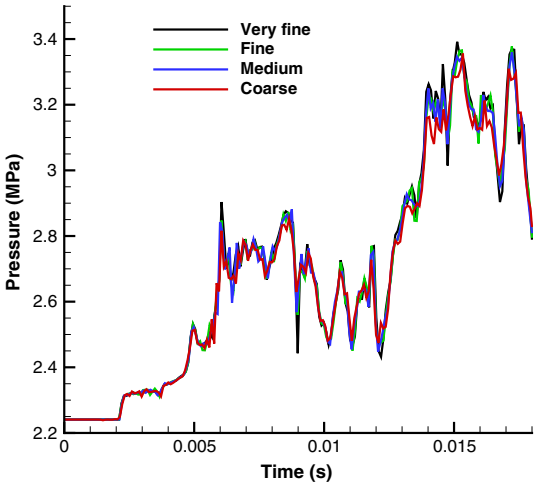

Fig. 23 Grid convergence study for active pressurization problem

force at the phase interface. Thus, the effect of the velocity non-equilibrium is relieved. A pressure wave is instantly propagating inside the tank, and the mixing between phases is vigorous enough to reach temperature equilibrium.

In order to obtain accurate monotonic solutions, the AUSMPW+_N scheme with the MLP5 limiter and the third-order TVD Runge–Kutta scheme are used for spatial and temporal discretizations, respectively. The effects of the phase change and turbulence are included via the cavitation model by Merkle and the $k-\omega$ SST model, respectively. The accommodation coefficients in the Merkle cavitation model are set to 10, and the time scale is determined as $R_{\text{tank}}/V_{\text{in}}$. As mentioned by Haselmaier et al. [44], active pressurization in this tank is a challenging CFD problem because it covers the entire regime of thermodynamic states from superheated gas and compressed liquids to supercritical mixtures. As the present multiphase solver fully couples the density and temperature in the energy equation and incorporates efficient and accurate real-fluid EOSs based on NIST data, the active pressurization in the LOX tank is successfully simulated.

Before actual computations, we firstly conducted the grid convergence study. Four different grids are used with equal wall spacing: coarse (17,000 cells), medium (26,000 cells), fine (34,000 cells), and very fine (42,000 cells). Figure 23 shows the initial pressure rise after the injection of non-condensable oxygen gas (i.e., incoming oxygen gas is not allowed to liquefy). Only the result of the coarse grid is quite

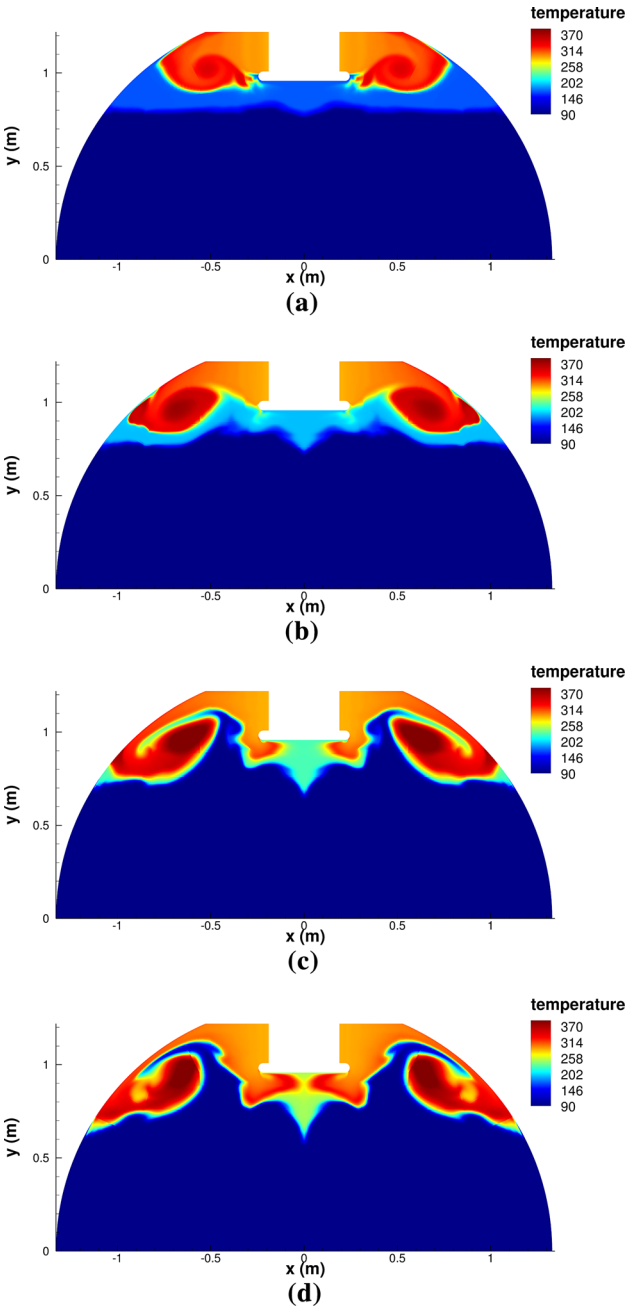

Fig. 24 Time evolution of the non-condensable N_2 injection. **a** $t = 0.05$ s. **b** $t = 0.1$ s. **c** $t = 0.2$ s. **d** $t = 0.3$ s

distant from other results. If the result of the very fine grid is assumed as standard, the RMS error of the coarse grid is 0.042 MPa, while the RMS errors of the medium and fine grid are 0.024 and 0.022 MPa, respectively. Since the RMS error of 0.027 MPa corresponds to the average 1% deviation from the result of the very find grid, we adopted the medium grid for computations.

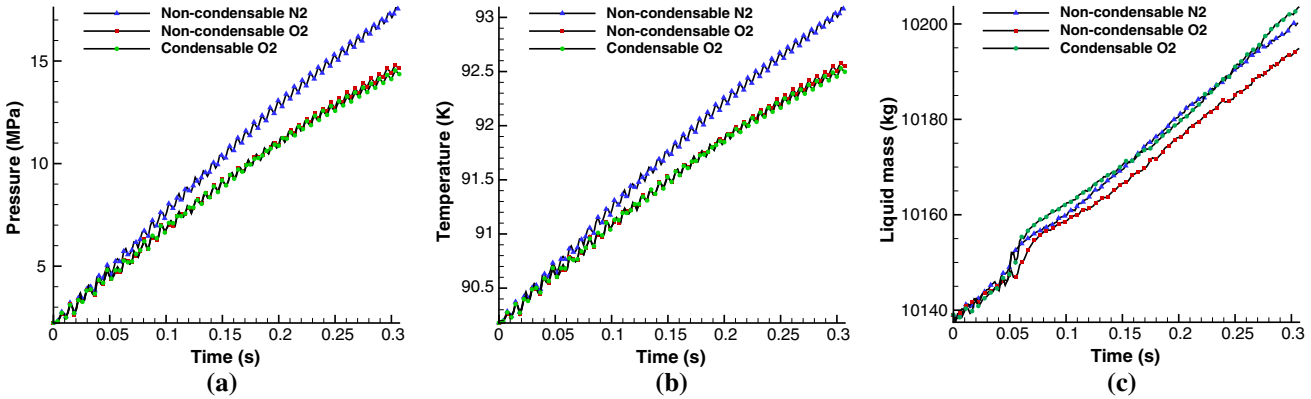

Fig. 25 Pressure, temperature, and liquid mass change inside the tank with different types of pressurant. **a** Pressure rise. **b** Liquid temperature rise. **c** Liquid mass change

5.2.1 Effect of pressurant type

In order to evaluate the effect of pressurant type on the pressure rise rate in the tank and to simulate realistic experimental scenarios, we consider three types of pressurant: non-condensable nitrogen, non-condensable oxygen, and condensable oxygen. The computations are then performed until $t = 0.3$ s in a zero-gravity environment.

Figure 24 displays the temperature distribution during the injection of non-condensable N_2. The flow injection generates a vortical flow, causing vigorous mixing inside the ullage. The liquid curls up along the vortex. The vortex grows until it reaches the tank wall, and then dissipates, distorting the liquid surface. As the numerical scheme is originally designed to capture contact discontinuities with low diffusion [24], it vividly portrays the mixing of the different species.

The other pressurants (non-condensable O_2 and condensable O_2) yield qualitatively similar flow patterns, but the pressure, temperature, and liquid/ullage mass are quantitatively different (see Fig. 25). The pressure and temperature increase rapidly inside the tank because the high-temperature gas is injected at a high mass flow rate. The supercritical ullage condenses into the liquid at the interface as it is cooled by the low-temperature liquid, thereby increasing the liquid mass. Although condensation decreases the amount of the vapor in the ullage, the ullage mass is increased by the high influx of mass from the diffuser (see Table 7).

Condensable O_2 yields the most condensation as in Fig. 25c and Table 7. This result is not surprising at all because condensable O_2 increases the amount of the vapor that can condense in the ullage. The difference between non-condensable N_2 and non-condensable O_2 can be explained by the lower molecular weight of N_2. Under the same mass flow rate condition, N_2 will be injected with higher velocity. The pressure increases more rapidly during the injection of non-condensable N_2 because N_2 gas molecules move faster than

Table 7 Mass increments during 0.3 s divided by the initial mass of each phase

Pressurant type	Liquid (%)	Ullage (%)
Non-condensable N_2	0.60	95.32
Non-condensable O_2	0.55	101.58
Condensable O_2	0.64	96.32

O_2 within the same confined volume (Fig. 25a). At the same time, ρC_p of N_2 is mostly lower than that of O_2 within the pressure and temperature range in this simulation, leading to a more rapid rise in the ullage temperature and thereby more energy exchange with the liquid (Fig. 25b). Near the cold liquid, the ullage containing N_2 gas with lower heat capacity condenses faster than the ullage containing non-condensable O_2 gas. Accordingly, among the three pressurants, non-condensable O_2 yields the highest mass increment in the ullage.

This comparative analysis of different pressurant types is rendered possible by the present numerical framework, which considers transport equation for the non-condensable gas phase in the governing equations.

5.2.2 Effect of gravity

Although the test facility is on the ground, we also investigate the effect of gravity on the active pressurization. For this purpose, the gravity is varied as 0, 0.01, and 1 g. The tank is then injected with non-condensable O_2, and the simulations are run up to 1.0 s.

Figure 26a, b shows the density distributions at $t = 1.0$ s under 0 and 0.01 g, respectively. The initially flat phase interface has been totally deformed. The interface is slightly more distorted under zero gravity than under microgravity. Figure 26c–e is the snapshots of the simulation under normal gravity at $t = 0.4$, 0.8, and 1.0 s, respectively. Unlike

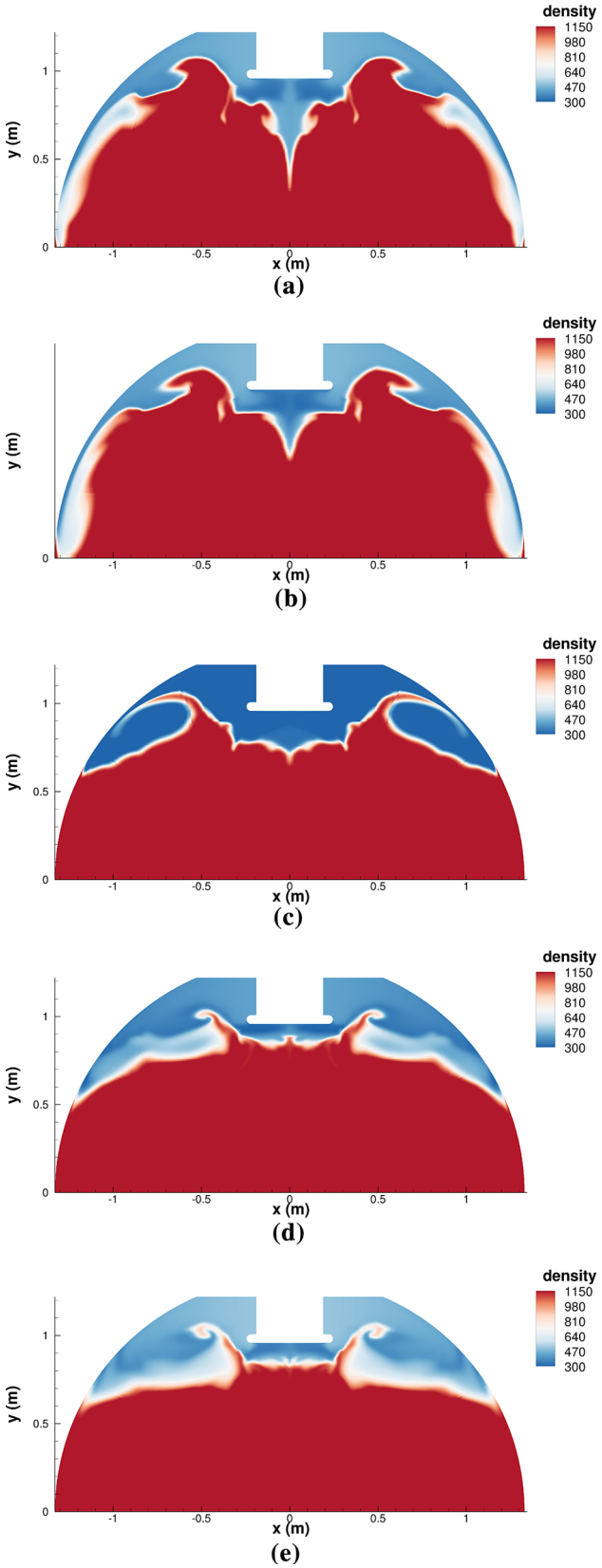

Fig. 26 Evolution of phase interface under different gravity conditions. **a** 0 g at $t = 1.0$ s. **b** 0.01 g at $t = 1.0$ s. **c** 1 g at $t = 0.4$ s. **d** 1 g at $t = 0.8$ s. **e** 1 g at $t = 1.0$ s

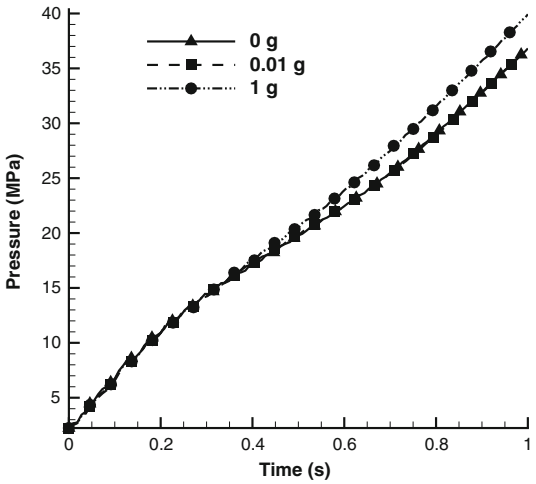

Fig. 27 Pressure rise under different gravity conditions

the results of zero gravity and microgravity, the vortex near the tank wall cannot penetrate the liquid phase; rather, the phase interface mostly regains its flatness at $t = 0.8$ s. This is attributed to the large hydrostatic pressure in the liquid region.

The flattened interface area in Fig. 26e is smaller than the distorted interface in Fig. 26a, b. The condensation occurs when the temperature of the supercritical ullage is lowered to the subcritical state by the contact with low-temperature liquid. Less condensation occurs under normal gravity due to the smaller phase interface area. Consequently, the ullage volume should be filled with a dense mixture of gases, which would increase the pressure inside the tank. The higher tank pressure under normal gravity at 1.0 s is confirmed in Fig. 27.

5.3 Unsteady cavitating flow around a 2-D wedge

Finally, we simulate the unsteady cavitating flows around a 2-D wedge. Similar to Sect. 5.1, the bulk liquid flow and small vapor bubbles play the roles of carrier and suspended phase. Thus, the homogeneous mixture approach is reasonable. The wedge shape can be modeled as the cross section of a control fin installed in high-speed underwater vehicles such as torpedoes. By analyzing the unsteady cavitating flows around a 2-D wedge, we can predict flow characteristics and hydrodynamic forces around the control fins of a high-speed underwater vehicle.

Two types of wedge are considered: one for natural cavitating flows and the other for ventilated cavitating flows. The geometric parameters are indicated in Fig. 28 and Table 8, respectively. Figure 29 shows the grid system and boundary conditions. As a spatial/temporal discretization method, we employ the RoeM_N scheme and the dual time-stepping with LU-SGS subiteration, respectively. The physical time step is $\Delta t = 1.0 \times 10^{-5}$ s. The Merkle cavitation model with

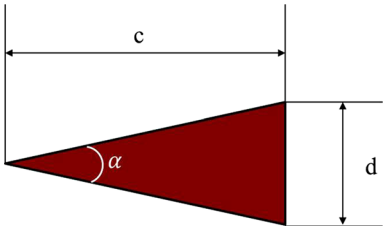

Fig. 28 Schematic of the wedge parameters

Table 8 Two types of wedge geometries

Case	Angle (α) (°)	Length (c) (mm)	Width (d) (mm)
Natural cavitation	20	56.72	20
Ventilated cavitation	20	35	12.34

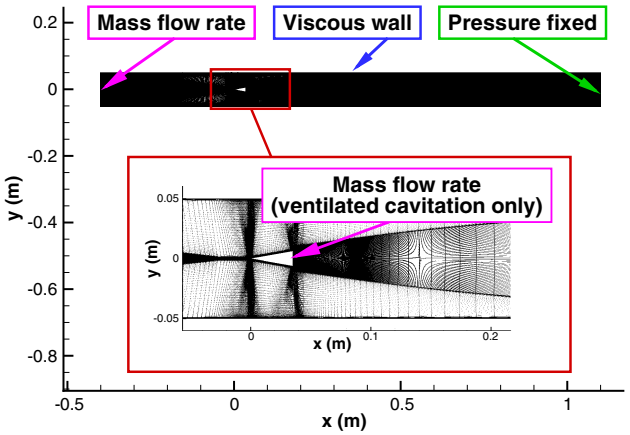

Fig. 29 Grid and boundary conditions in the 2-D wedge simulation

$C_{vp} = C_{cd} = 100$ and time scale of d/V_∞ is employed. For the effects of turbulence, $k-\omega$ SST model is adopted.

5.3.1 Comparison with the experimental data

The computational results are compared with the experimental data obtained from Chungnam National University Cavitation Tunnel (CNU-CT). Table 9 presents the experimental flow conditions for comparison. Cavitation numbers vary according to the free stream pressure in natural cavitating flows, while those in ventilated cavitating flows are controlled by the ventilated mass flow rate ($\dot{m}$). It is noted that the cavitation number for the ventilated cavitation (σ_v) is calculated using the pressure inside the ventilated cavity instead of the saturation pressure used in the original definition of the cavitation number (σ).

$$\sigma = \frac{p_\infty - p_{sat}}{0.5\rho_\infty V_\infty^2}, \tag{77}$$

$$\sigma_v = \frac{p_\infty - p_{cavity}}{0.5\rho_\infty V_\infty^2}. \tag{78}$$

Table 9 Experimental flow conditions

Natural cavitation				
p_∞ (kPa)	61.96	52.96	39.14	31.56
V_∞ (m/s)	8.3	8.3	8.3	8.3
$\dot{m}$ (g/s)	–	–	–	–
σ	1.75	1.49	1.09	0.87
Ventilated cavitation				
p_∞ (kPa)	89	89	89	89
V_∞ (m/s)	6.0	6.0	6.0	6.0
$\dot{m}$ (g/s)	1.66	2.10	2.32	4.7
σ_v	0.90	0.80	0.70	0.58

Figure 30 shows the snapshots of experiment and numerical schlieren for the shedding vortices at each cavitation number. Unlike the results of natural cavitating flows, non-condensable gas ejected behind the wedge forms cavities, and they last longer in ventilated cavitating flows. There is a slight difference (about 2% difference) in the cavitation number between computations and experiments, because it is difficult to exactly match unsteady upstream pressure due to random pressure fluctuations existing in the computational domain. All results show similar patterns of the shedding vortices between experiments and computations. As we show in Fig. 30, characteristics of natural and ventilated cavitating flows do not coincide with each other at similar cavitation numbers. This is because the two wedges have different sizes and shapes. However, Fig. 31 shows that the natural and ventilated cavitating flows have analogous non-dimensional length of cavities at the similar cavitation number. Again, there is a good agreement between computational predictions and experimental measurements for both natural and ventilated cavitating flows.

5.3.2 Effect of cavitation on the drag coefficient

To examine the effect of cavitation on the drag force exerted to the wedge, the drag coefficient in terms of the cavitation number is shown in Fig. 32. As the flow unsteadiness becomes stronger at higher cavitation number, the length of error bar (or the degree of uncertainty) increases. For natural cavitating flows, the free stream pressure is lowered to reduce the cavitation number (77), so the drag coefficient based on the pressure difference between the front and back of the wedge is also reduced (Fig. 32a). In the case of ventilated cavitating flows, cavitation numbers are regulated by the ventilated mass flow rate of air. As shown in Fig. 30b and Table 9, a large amount of the ventilated mass flow rate forms a streamlined cavity behind the wedge, reducing the pressure drag and cavitation number (Fig. 32b).

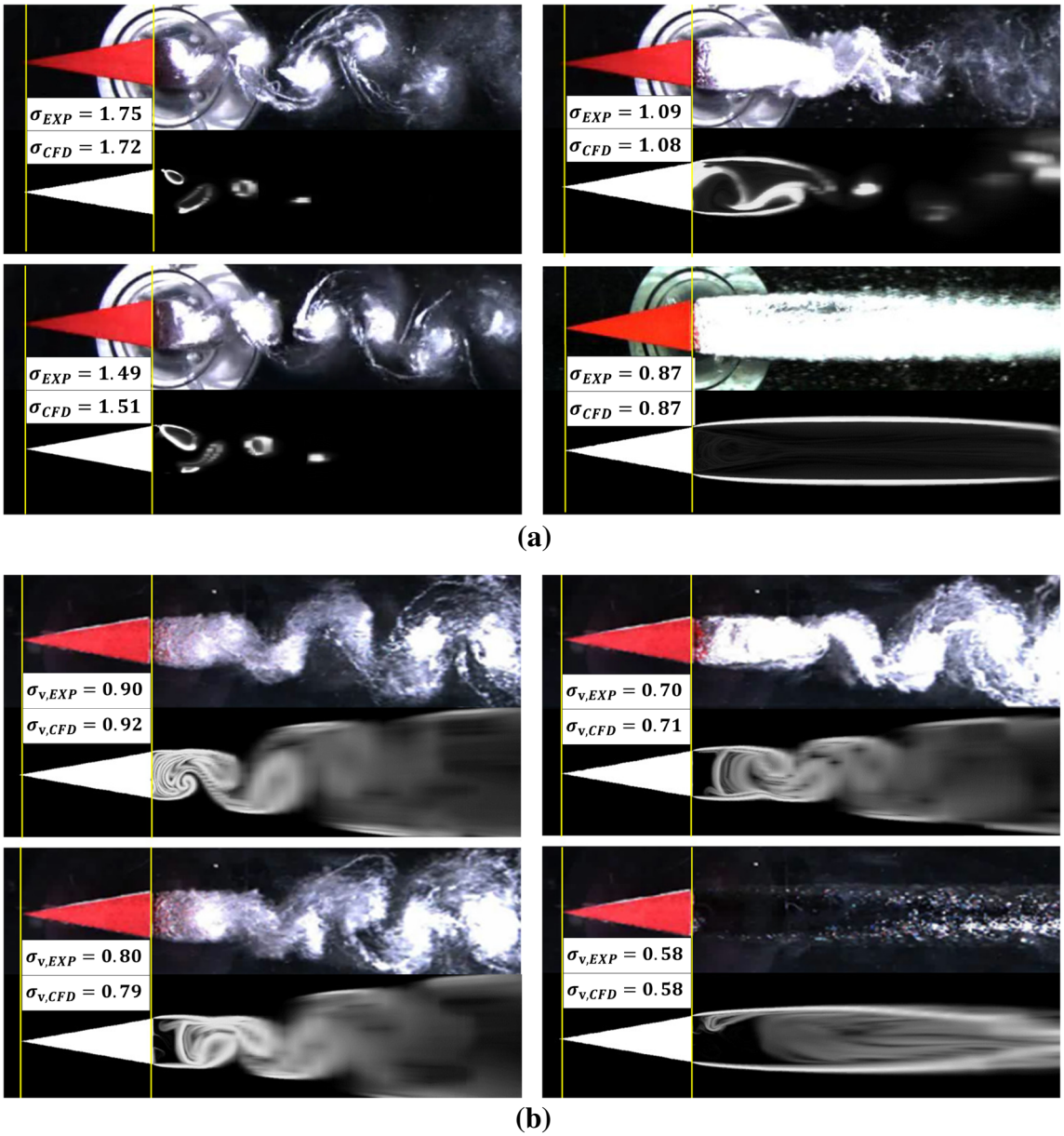

Fig. 30 Snapshots of cavitating flows at each cavitation number. **a** Natural cavitating flows. **b** Ventilated cavitating flows

Figure 33 represents the drag coefficient curve over the free stream velocity. As the free stream velocity increases without ventilation, natural cavitation starts to happen, thereby reducing the drag coefficient. In the low-speed region where natural cavitation does not occur, the drag coefficient can be substantially reduced by the ventilated air. In this case, the drag coefficients are obtained without fluctuation because the ventilated mass flow rate is large enough to form a steady cavity. This result can be exploited to underwater vehicles; an underwater vehicle in low-speed region can reduce its drag by the ventilated air at the back of the control fins in order to achieve high speed.

6 Conclusion

Numerical issues that must be settled for computing multiphase problems have been addressed. First, a proper model for multiphase flows has been selected; the homogeneous mixture approach is computationally efficient without sacrificing physical reality when the relevant equilibrium assumptions are legitimate, and the extension of single-phase numerical schemes to multiphase within the homogeneous mixture framework is relatively tractable. Enhanced convective flux schemes for multiphase real-fluid flows over a wide range of flow speeds (the AUSMPW+_N and RoeM_N schemes) have been developed with system preconditioning.

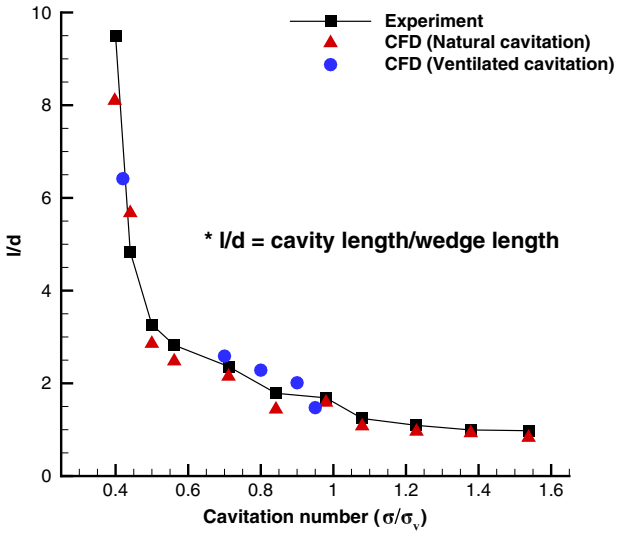

Fig. 31 Non-dimensional length of cavities as a function of the cavitation number

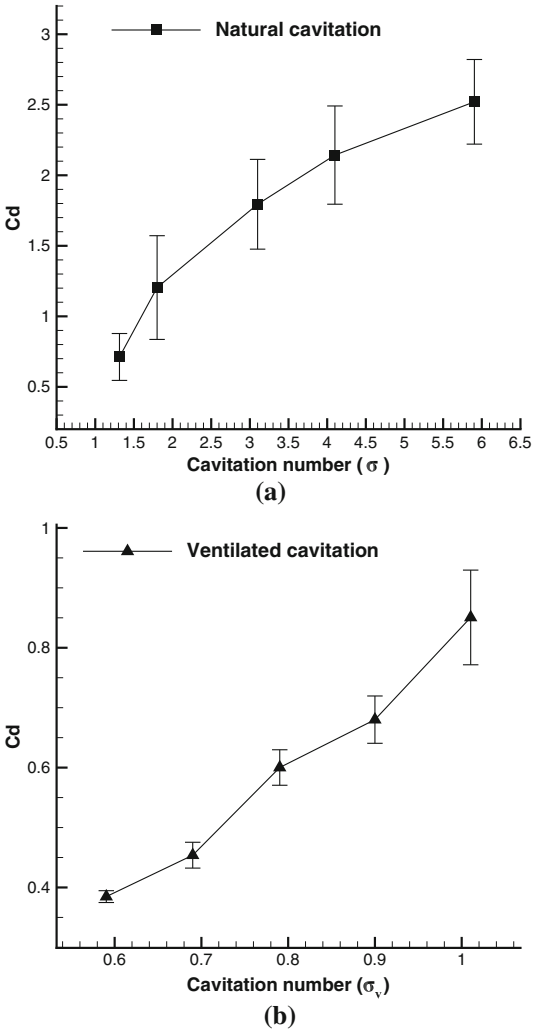

Fig. 32 Drag coefficients as a function of the cavitation number. **a** Natural cavitating flows. **b** Ventilated cavitating flows

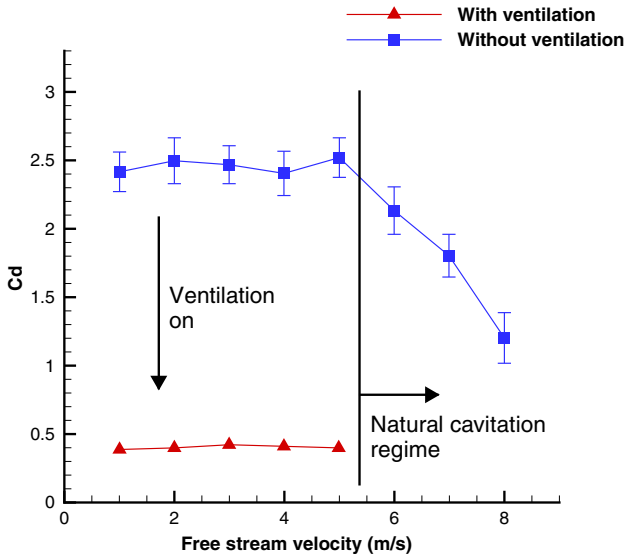

Fig. 33 Drag coefficients as a function of the natural and ventilated cavitation over the free stream velocity

As a result, depending on the working fluid and operating condition, a suitable EOS can be chosen for each problem. Phase change phenomenon that also requires prudent choice of modeling has been dealt with appropriate cavitation model or nucleation model. The accuracy and robustness of the proposed numerical methods and physical models have been confirmed with extensive validation problems, ranging from compressible air/water shock-tube tests to phase change in real-fluid flows.

After validation, various application problems have been computed with the same numerical framework. The experimental measurement on the suction performance of TVC has been accurately predicted. Complex flow physics associated with multiphase shocks and phase changes have been successfully simulated through accurate and robust numerical methods. Injection of a pressurizing agent in a cryogenic tank has been computed, and the flow characteristics during the pressurization process have been analyzed. Covering the entire range of thermodynamic states inside the tank is accomplished owing to the compressible homogeneous mixture framework incorporated with the real-fluid EOS. Finally, numerical simulations of unsteady cavitating flows around a 2-D wedge have been carried out. The computational results have shown similar characteristics with the experimental measurements for both natural and ventilated cavitating flows, representing the accuracy of the numerical schemes in unsteady multiphase flows where incompressible and compressible regions coexist.

Accurate numerical methods with proper physical modeling make it possible to explore a broad spectrum of multiphase phenomena with computations. Unlike the current commercial and/or open-source packages which are

mostly based on pressure-based solvers, the proposed numerical framework can provide the robust and accurate treatment of multiphase shocks and phase interfaces. As the next step, the proposed numerical methods will be extended to three-dimensional multiphase flows with more complex and realistic problems.

Acknowledgements This research is supported by the program of National Research Foundation of Korea (NRF-2014M1A3A3A0203-4856), by Advanced Research Center Program (NRF-2013R1A5A107-3861) through the National Research Foundation of Korea (NRF) Grant funded by the Korea government (MSIP) contracted through Advanced Space Propulsion Research Center at Seoul National University, and by the Civil-Military Technology Cooperation Program. This work is also supported by the KISTI Supercomputing Center (KSC-2016-C3-0067, KSC-2017-G2-0004). The authors appreciate the valuable experimental data provided by Doosan Heavy Industries and Chungnam National University Cavitation Tunnel (CNU-CT). Finally, the comments and suggestions of the reviewers on the original manuscript are highly appreciated.

References

1. Baer, M.R., Nunziato, J.W.: A two-phase mixture theory for the deflagration-to-detonation transition (DDT) in reactive granular materials. Int. J. Multiph. Flows **12**, 861–889 (1986). doi:10.1016/0301-9322(86)90033-9
2. Romenski, E., Resnyansky, A.D., Toro, E.F.: Conservative hyperbolic formulation for compressible two-phase flow with different phase pressures and temperatures. Q. Appl. Math. **65**(2), 259–279 (2007). doi:10.1090/S0033-569X-07-01051-2
3. Zeidan, D.: Assessment of mixture two-phase flow equations for volcanic flows using Godunov-type methods. Appl. Math. Comput. **272**, 707–719 (2016). doi:10.1016/j.amc.2015.09.038
4. Bruce Stewart, H., Wendroff, B.: Two-phase flow: Models and methods. J. Comput. Phys. **56**(3), 363–409 (1984). doi:10.1016/0021-9991(84)90103-7
5. Liou, M.S., Chang, C.H., Nguyen, L., Theofanous, T.G.: How to solve compressible multifluid equations: a simple, robust, and accurate method. AIAA J. **46**(9), 2345–2356 (2008). doi:10.2514/1.34793
6. Saurel, R., Le Metayer, O., Massoni, J., Gavrilyuk, S.: Shock jump relations for multiphase mixtures with stiff mechanical relaxation. Shock Waves **16**(3), 209–232 (2007). doi:10.1007/s00193-006-0065-7
7. Hosangadi, A., Ahuja, V.: Numerical study of cavitation in cryogenic fluids. J. Fluids Eng. **127**(2), 267–281 (2005). doi:10.1115/1.1883238
8. Kunz, R.F., Boger, D.A., Stinebring, D.R., Chyczewski, T.S., Lindau, J.W., Gibeling, H.J., Venkateswaran, S., Govindan, T.: A preconditioned Navier–Stokes method for two-phase flows with application to cavitation prediction. Comput. Fluids **29**(8), 849–875 (2000). doi:10.1016/S0045-7930(99)00039-0
9. Saurel, R., Boivin, P., Le Métayer, O.: A general formulation for cavitating, boiling and evaporating flows. Comput. Fluids **128**, 53–64 (2016). doi:10.1016/j.compfluid.2016.01.004
10. Utturkar, Y., Wu, J., Wang, G., Shyy, W.: Recent progress in modeling of cryogenic cavitation for liquid rocket propulsion. Prog. Aerosp. Sci. **41**(7), 558–608 (2005). doi:10.1016/j.paerosci.2005.10.002
11. Kim, H., Kim, H., Kim, C.: Computations for homogeneous multiphase real fluid flows at all speeds. AIAA J. (2018). doi:10.2514/1.J056497
12. Flåtten, T., Lund, H.: Relaxation two-phase flow models and the subcharacteristic condition. Math. Models Methods Appl. Sci. **21**(12), 2379–2407 (2011). doi:10.1142/S0218202511005775
13. Harlow, F.H., Amsden, A.A.: Fluid Dynamics: A LASL Monograph. Technical Report LA-4700, Los Alamos, New Mexico (1971)
14. Wagner, W., Kretzschmar, H-J.: International steam tables: properties of water and steam based on the industrial formulation IAPWS-IF97. In: IAPWS Industrial Formulation 1997 for the Thermodynamic Properties of Water and Steam, pp. 7–150. Springer, Berlin, Heidelberg (2008). doi:10.1007/978-3-540-74234-0_3
15. NIST: NIST reference fluid thermodynamic and transport properties database (REFPROP): version 8.0. http://www.nist.gov/srd/nist23.cfm (2010)
16. Kunick, M., Kretzschmar, H.-J.: Guideline on the fast calculation of steam and water properties with the spline-based table look-up method (SBTL). Technical Report, The International Association for the Properties of Water and Steam (2015)
17. Merkle, C.L., Feng, J.Z., Buelow, P.E.O.: Computational modeling of the dynamics of sheet cavitation. In: 3rd International Symposium on Cavitation. Grenoble, France (1998)
18. Sauer, J., Schnerr, G.H.: Unsteady cavitating flow—a new cavitation model based on modified front capturing method and bubble dynamics. In: Summer Meeting, American Society of Mechanical Engineers; Fluids Engineering Division. American Society of Mechanical Enginners, Boston, Massachusetts (2000)
19. Hertz, H.: Ueber die Verdunstung der Flüssigkeiten, insbesondere des Quecksilbers, im luftleeren Raume. Ann. Phys. **253**, 177–193 (1882). doi:10.1002/andp.18822531002
20. Hill, P.G.: Condensation of water vapour during supersonic expansion in nozzles. J. Fluid Mech. **25**(03), 593–620 (1966). doi:10.1017/S0022112066000284
21. Menter, F.R., Kuntz, M., Langtry, R.: Ten years of industrial experience with the SST turbulence model. Turbul. Heat Mass Transf. **4**, 625–632 (2003)
22. Weiss, J.M., Smith, W.A.: Preconditioning applied to variable and constant density flows. AIAA J. **33**(11), 2050–2057 (1995). doi:10.2514/3.12946
23. Venkateswaran, S., Merkle, C.L.: Dual time-stepping and preconditioning for unsteady computations. In: 33rd Aerospace Sciences Meeting and Exhibit, Aerospace Sciences Meetings. American Institute of Aeronautics and Astronautics, Reno, Nevada, AIAA Paper 1995-78 (1995). doi:10.2514/6.1995-78
24. Kim, K.H., Kim, C., Rho, O.H.: Methods for the accurate computations of hypersonic flows: I. AUSMPW+ Scheme. J. Comput. Phys. **174**(1), 38–80 (2001). doi:10.1006/jcph.2001.6873
25. Kim, S., Kim, C., Rho, O.H., Hong, S.K.: Cures for the shock instability: Development of a shock-stable Roe scheme. J. Comput. Phys. **185**(2), 342–374 (2003). doi:10.1016/S0021-9991(02)00037-2
26. Liou, M.S.: A sequel to AUSM, Part II: AUSM$^+$-up for all speeds. J. Comput. Phys. **214**(1), 137–170 (2006). doi:10.1016/j.jcp.2005.09.020
27. Ihm, S.W., Kim, C.: Computations of homogeneous-equilibrium two-phase flows with accurate and efficient shock-stable schemes. AIAA J. **46**(12), 3012–3037 (2008). doi:10.2514/1.35097
28. Roe, P.: Approximate Riemann solvers, parameter vectors, and difference schemes. J. Comput. Phys. **43**(2), 357–372 (1981). doi:10.1016/0021-9991(81)90128-5
29. Gottlieb, S., Shu, C.W.: Total variation diminishing Runge–Kutta schemes. Math. Comput. **67**(221), 73–85 (1998). doi:10.1090/S0025-5718-98-00913-2
30. Yoon, S., Jameson, A.: Lower–upper symmetric-Gauss–Seidel method for the Euler and Navier–Stokes equations. AIAA J. **26**(9), 1025–1026 (1988). doi:10.2514/3.10007

31. Yoon, S.H., Kim, C., Kim, K.H.: Multi-dimensional limiting process for three-dimensional flow physics analyses. J. Comput. Phys. **227**(12), 6001–6043 (2008). doi:10.1016/j.jcp.2008.02.012
32. Quirk, J.J.: A contribution to the great Riemann solver debate. Int. J. Numer. Meth. Fluids **18**, 555–574 (1994). doi:10.1002/fld.1650180603
33. Kitamura, K., Liou, M.S., Chang, C.H.: Extension and comparative study of AUSM-family schemes for compressible multiphase flow simulations. Commun. Comput. Phys. **16**(3), 632–674 (2014). doi:10.4208/cicp.020813.190214a
34. Müller, B.: Low-Mach-number asymptotics of the Navier–Stokes equations. J. Eng. Math. **34**(1), 97–109 (1998). doi:10.1023/A:1004349817404
35. Pelanti, M.: Low Mach number preconditioning techniques for Roe-type and HLLC-type methods for a two-phase compressible flow model. Appl. Math. Comput. **310**, 112–133 (2017). doi:10.1016/j.amc.2017.04.014
36. Meng, H., Yang, V.: A unified treatment of general fluid thermodynamics and its application to a preconditioning scheme. J. Comput. Phys. **189**(7), 277–304 (2003). doi:10.1016/S0021-9991(03)00211-0
37. Abgrall, R.: How to prevent oscillations in multicomponent flow calculations: A quasi conservative approach. J. Comput. Phys. **125**(1), 150–160 (1996). doi:10.1006/jcph.1996.0085
38. Lee, B.J., Toro, E.F., Castro, C.E., Nikiforakis, N.: Adaptive Osher-type scheme for the Euler equations with highly nonlinear equations of state. J. Comput. Phys. **246**, 165–183 (2013). doi:10.1016/j.jcp.2013.03.046
39. Shyue, K.M.: A fluid-mixture type algorithm for compressible multicomponent flow with van der Waals equation of state. J. Comput. Phys. **156**(1), 43–88 (1999). doi:10.1006/jcph.1999.6349
40. Hord, J.: Cavitation in Liquid Cryogens II: Hydrofoil. Technical Report CR-2156, Cleveland, Ohio (1973)
41. Moore, M.J., Walters, P.T., Crane, R.I., Davidson, B.J.: Predicting the fog drop size in wet steam turbines. Wet Steam **4**, 101–109 (1973)
42. Kermani, M.J., Gerber, A.G.: A general formula for the evaluation of thermodynamic and aerodynamic losses in nucleating steam flow. Int. J. Heat Mass Transf. **46**(17), 3265–3278 (2003). doi:10.1016/S0017-9310(03)00096-6
43. Ahuja, V., Hosangadi, A., Mattick, S., Lee, C.P., Field, R.E., Ryan, H.: Computational analyses of pressurization in cryogenic tanks. In: 44th AIAA/ASME/SAE/ASEE Joint Propulsion Conference & Exhibit. Hartford, CT, AIAA Paper 2008-4752 (2008). doi:10.2514/6.2008-4752
44. Haselmaier, L.H., Field, R.E., Ryan, H.M., Dickey, J.C.: Overview of propellant delivery systems at the NASA John C. Stennis Space Center. In: 42nd AIAA/ASME/SAE/ASEE Joint Propulsion Conference & Exhibit, AIAA Paper 2006-4757 (2006). doi:10.2514/6.2006-4757